National Library of Canada | Bibliothèque nationale du Canada

Canadian Theses Service | Service des thèses canadiennes

Ottawa, Canada
K1A 0N4

NOTICE

The quality of this microform is heavily dependent upon the quality of the original thesis submitted for microfilming. Every effort has been made to ensure the highest quality of reproduction possible.

If pages are missing, contact the university which granted the degree.

Some pages may have indistinct print especially if the original pages were typed with a poor typewriter ribbon or if the university sent us an inferior photocopy.

Previously copyrighted materials (journal articles, published tests, etc.) are not filmed.

Reproduction in full or in part of this microform is governed by the Canadian Copyright Act, R.S.C. 1970, c. C-30.

AVIS

La qualité de cette microforme dépend grandement de la qualité de la thèse soumise au microfilmage. Nous avons tout fait pour assurer une qualité supérieure de reproduction.

S'il manque des pages, veuillez communiquer avec l'université qui a conféré le grade.

La qualité d'impression de certaines pages peut laisser à désirer, surtout si les pages originales ont été dactylographiées à l'aide d'un ruban usé ou si l'université nous a fait parvenir une photocopie de qualité inférieure.

Les documents qui font déjà l'objet d'un droit d'auteur (articles de revue, tests publiés, etc.) ne sont pas microfilmés.

La reproduction, même partielle, de cette microforme est soumise à la Loi canadienne sur le droit d'auteur, SRC 1970, c. C-30.

THE UNIVERSITY OF ALBERTA

CARRIER TRANSPORT IN MAGNETOTRANSISTORS

BY

AROKIA NATHAN

A THESIS

SUBMITTED TO THE FACULTY OF GRADUATE STUDIES AND RESEARCH

IN PARTIAL FULFILLMENT OF THE REQUIREMENTS FOR THE DEGREE OF

DOCTOR OF PHILOSOPHY

DEPARTMENT OF ELECTRICAL ENGINEERING

EDMONTON, ALBERTA

FALL 1988

Permission has been granted to the National Library of Canada to microfilm this thesis and to lend or sell copies of the film.

L'autorisation a été accordée à la Bibliothèque nationale du Canada de microfilmer cette thèse et de prêter ou de vendre des exemplaires du film.

The author (copyright owner) has reserved other publication rights, and neither the thesis nor extensive extracts from it may be printed or otherwise reproduced without his/her written permission.

L'auteur (titulaire du droit d'auteur) se réserve les autres droits de publication; ni la thèse ni de longs extraits de celle-ci ne doivent être imprimés ou autrement reproduits sans son autorisation écrite.

ISBN 0-315-45488-1

THE UNIVERSITY OF ALBERTA

RELEASE FORM

NAME OF AUTHOR: Arokia Nathan

TITLE OF THESIS: Carrier Transport in Magnetotransistors

DEGREE: Doctor of Philosophy

YEAR THIS DEGREE GRANTED: 1988

Permission is hereby granted to THE UNIVERSITY OF ALBERTA LIBRARY to reproduce single copies of this thesis and to lend or sell such copies for private, scholarly or scientific research purposes only.

The author reserves other publication rights, and neither the thesis nor extensive extracts from it may be printed or otherwise reproduced without the author's written permission.

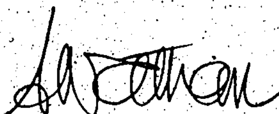

Student's signature

11 Tan Iu Ghee Road

Penang 10460

W. Malaysia

Date: May 3, 1988

THE UNIVERSITY OF ALBERTA

FACULTY OF GRADUATE STUDIES AND RESEARCH

The undersigned certify that they have read, and recommend to the Faculty of Graduate Studies and Research for acceptance, a thesis entitled *Carrier Transport in Magnetotransistors*, submitted by Arokia Nathan, in partial fulfillment of the requirements for the degree of *Doctor of Philosophy*.

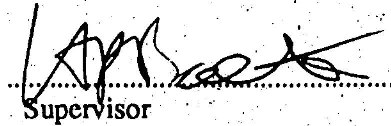

Supervisor

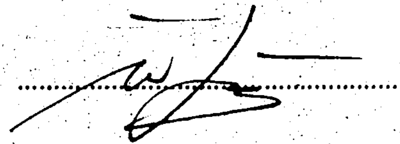

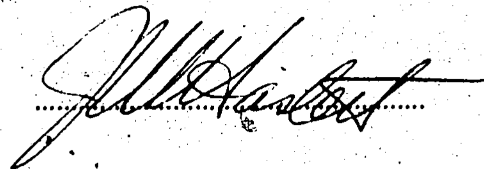

Date: April 18, 1988

Abstract

The analysis of galvanomagnetic carrier transport in magnetic-field-sensitive integrated bipolar transistors is presented. Based on a two-dimensional numerical model that employs a finite box procedure, high resolution computations (± 0.5 μV stopping criterion) of the potentials in the base region of magnetotransistors were performed for realistic device structures and operating conditions. The results show that the magnitude of Hall fields at the emitter base junction vicinity, are too minute to cause any appreciable asymmetric minority carrier injection, hence invalidating the widely invoked emitter injection modulation model. Measured data obtained using novel Hall probes procedures are in support of the conclusions derived from the numerical model. Carrier deflection appears to be the prevailing operating principle for magnetotransistors with a linear output response, while magnetoconcentration seems to be adequate to describe possible nonlinearities. Measurements results of $1/f$ noise in dual-collector magnetotransistors are also presented. In particular, a strong positive correlation (close to 100 %) between the noise voltages of the collectors, has been observed. This unique correlation in the noise voltages indicates that a field resolution of 22 μT over a 5 MHz bandwidth is possible, with a magnetotransistor of a mere 6 %/T sensitivity operating in the differential mode with less than 1 mA of total current. The correlation of the collector noise voltages seems to be independent of fabrication technology.

ACKNOWLEDGEMENTS

It is a pleasure to thank my supervisor, Dr. H. P. Baltes whose continuous motivation and inspiration made this challenging piece of research very enjoyable. I would also like to thank Dr. Walter Allegretto (University of Alberta) for the numerous number of stimulating discussions and encouraging moments, and the various collaborators in Canada, Italy, and Japan for their technical support.

My sincere thanks to the Izaak Walton Killam Scholarship fund for providing the necessary financial assistance.

Table of Contents

Chapter Page

1. Introduction 1
2. Previous Magnetotransistor Analysis 5
   2.1 Hall Effect 5
   2.2 Carrier Deflection 8
   2.3 Magnetoconcentration 10
3. Model Equations for Magnetotransistor Simulation 11
   3.1 Poisson's Equation and Continuity Eqations 11
   3.2 Galvanomagnetic Transport Equations 11
   3.3 The Basic System 19
   3.4 Boundary and Interface Conditions 20
   3.5 Physical Models 21
4. Numerical Procedure 23
   4.1 Discretisation Scheme 23
      4.1.1 Poisson's Equation 23
      4.1.2 Carrier Continuity Equations 25
   4.2 Solution Scheme 29
   4.3 Evaluation of Terminal Currents 31
5. Galvanomagnetic Carrier Transport Analysis 35
   5.1 Simulation Results for Emitter Base Junctions 35
   5.2 Simulation Results for Dual-Collector Magnetotransistors 37
   5.3 Measurement of Hall Voltage at Emitter Base Junction 37
   5.4 Experimental Results for MT in Common-Base Configuration 39
   5.5 Numerical and Experimental Results for MT in Common-Emitter Diode Configuration 41
      5.5.1 Discussion of Numerical Results 41
      5.5.2 Discussion of Measurement Results 43

5.5.3 Comparison of Numerical and Measurement Results 44

6. 1/f Noise in Magnetotransistors 61

6.1 Previous Noise Studies in Magnetotransistors 61

6.2 Device Description 62

6.3 Measurement Procedure 63

6.4 Correlation in Collector Noise Voltages 66

CONCLUSIONS AND OUTLOOK 71

REFERENCES 74

APPENDIX 1. Partial Linearisation of Continuity Equations 79

APPENDIX 2. Procedure for Predicting Trial Values of Potentials 80

List of Figures

Figure		Page
4.1	Triangular mesh for an emitter base junction of a magnetotransistor, generated using Delauney triangulation at junction sidewalls and regular grid triangulation everywhere else.	33
4.2	The cell or subdomain, Ω_i (bounded by $\partial\Omega_i$) formed by the union of perpendicular bisectors of elemental edges converging to node i.	34
4.3	An element with vertices i, j, and k, constituting part of the cell shown in Fig. 4.2. The notation used is described in the text.	34
5.1	Two-dimensional geometry of device enclosed by an artificial oxide region.	47
5.2	(a) Equipotential lines and (b) potential distribution in the domain shown in Fig. 5.1.	47
5.3	Flow lines of current density for: (a) electrons injected from the emitter, (b) holes injected from base.	48
5.4	The distribution of (a) electrons and (b) holes in the domain as shown in Fig. 5.2. The distributions have been clipped off at 10^{19} cm^{-3} at the respective N+ and P+ regions. In the oxide region, electron and hole concentrations are zero. Note that the direction of axes are opposite in both cases.	48
5.5	Two-dimensional geometry of diode. AA' and BB' denote cut lines at $x = 6.75$ μm and $x = 5$ μm respectively.	49
5.6	Electrostatic potential distribution in diode (5 μm $\leq y \leq$ 15 μm) at BB' and AA'. Device is operated at high injection, $V_{BE} = 0.9$ V, and $B = 2$ Tesla.	49
5.7	Electron and hole concentrations in device at BB' operated at high injection. Operating conditions of device as in Fig. 5.6.	49
5.8	Simulation geometry of dual-collector NPN magnetotransistor.	50
5.9	Potential distribution for $V_{BE} = V_{CE} = 0.9$ V, and $B = 0$ T.	50
5.10	(a) Equipotential lines. Current density flow lines of (b) holes injected from base (c) electrons injected from emitter. $V_{BE} = V_{CE} = 0.9$ V, and $B = 0$ T.	51
5.11	As in Fig. 5.10, but for $B = 2$ Tesla.	51
5.12	Measurement schematic of differential voltage, V_D across the emitter base junction of the SSIMT. The magnetic induction, B is perpendicular to the direction of the injected current.	52

5.13 The differential voltage as a function of magnetic induction ($|B| \leq 0.9$ T) for various emitter currents. 52

5.14 (a) Top view and (b) cross-sectional view of the basic bipolar, dual-collector MT geometry used in the measurements. 53

5.15 The measured impurity profile at $x = 0$ for the device shown in Fig. 5.14. The profile used in simulations is discussed in Section 5.5.1. 54

5.16 Current voltage characteristics for the MT in common-base configuration. The emitter current is in steps of 200 μA. 54

5.17 Collector current imbalance, $\Delta I_C = (I_{C1} - I_{C2})$ as a function of field strength for $|B| \leq 200$ mT. The device is operated at $V_{CB} = 5$ V and $I_E = -1$ mA. 55

5.18 The Hall voltage measured as a function of magnetic induction ($|B| \leq 250$ mT) for the MT with $W' = 40$ μm. The operating conditions of device are as in Fig. 5.17. 55

5.19 As in Fig. 5.18 but for the MT's with $W' = 60$ μm and 80 μm. 56

5.20 Comparison of Hall voltages as a function of magnetic induction, obtained from the analytical model and measured using the MT with $W' = 40$ μm. The MT is operated at $V_{CB} = 5$ V and $I_E = -1$ mA. 56

5.21 Two-dimensional simulation geometry of the MT's base region surrounded by an artificial oxide region. 57

5.22 The Hall voltage distribution as a function of position, W' (see Fig. 5.21) along $y = 0$, for various base emitter voltages and $B = 500$ mT. 57

5.23 The Hall voltage as a function of position at various field strengths for $V_{BE} = 0.85$ V. 57

5.24 Equipotential lines in the vicinity of the emitter for $V_{BE} = 0.85$ V and $B = 2$ T. The displayed area corresponds to $|x| \leq 14.5$ μm and -1 μm $\leq |y| \leq 4.5$ μm; see Fig. 5.21 for x and y orientations. 58

5.25 Minority carrier (electron) flow lines in the vicinity of the emitter for $V_{BE} = 0.85$ V and $B = 2$ T. The displayed area corresponds to $|x| \leq 11$ μm and $0 \leq |y| \leq 4.5$ μm; see Fig. 5.21 for x and y orientations. 58

5.26 The Hall voltage monitored as a function of injection level at $B = 500$ mT for the various MT geometries. 59

5.27 Comparison of measured and simulated current-voltage characteristics for MT in common-emitter diode configuration. 59

5.28 Comparison of measured and simulated (ideal) Hall voltages for $V_{BE} = 0.7$ V and $B = 500$ mT. 60

5.29 As in Fig. 5.28 but for $V_{BE} = 0.75$ V. 60

5.30 As in Fig. 5.28 but for $V_{BE} = 0.8$ V. 60

6.1 Cross-sectional view of CMOS magnetotransistor sensitive to fields parallel to chip surface. 69

6.2 Schematic of noise measurement system. 69

6.3 Noise voltage power spectral density of low noise amplifier operated in single ended and differential modes with 221 kΩ resistors at amplifier inputs. 69

6.4 The single ended and differential collector noise voltage PSD's for the MT fabricated in CMOS technology. 70

6.5 As in Fig. 6.4 but for MT fabricated in bipolar technology. 70

NOMENCLATURE

Symbol	Description
B	magnetic induction vector
B_{min}	magnetic field resolution
$D_{n,p}$	electron and hole diffusion constants
E	electric field vector
E	energy
E_f	Fermi energy
I_E, I_B, I_C	emitter, base and collector currents
J_e, J_q	electric and heat current density vectors
J_n, J_p	electron and hole current density vectors
J_{nB}, J_{pB}	magnetic field dependent electron and hole current density vectors
N	net ionised impurity concentration
N_A, N_D	acceptor and donor impurity concentrations
N_T	total ionised impurity concentration
R_λ	net recombination rate
R_H	Hall coefficient
S	sensitivity to the magnetic field in terms of relative current imbalance
$S(\omega)$	power spectral density of noise voltage, $v_n(t)$
$V_n(\omega)$	Fourier transform of $v_n(t)$
$V^*_n(\omega)$	complex conjugate of $V_n(\omega)$
T	temperature
V_{BE}	base emitter voltage
V_{CE}	collector emitter voltage

V_H	Hall voltage
V_T, V_t	thermal voltage, kT/q
h	Planck constant (6.626176×10^{-34} VAs^2)
k	Boltzmann's constant (1.380662×10^{-23} VAsK^{-1})
n, p	electron and hole concentrations
n_i	intrinsic concentration
q	elementary charge ($1.6021892 \times 10^{-19}$ As)
f	frequency
$v_n(t)$	noise voltage
x_j	junction depth
Δf	frequency bandwidth
ε	material permittivity
θ	Hall angle
$\varphi_{n,p}$	electron and hole Fermi potentials
ψ	electrostatic potential
ρ	space charge
τ	relaxation time
$\tau_{n,p}$	electron and hole lifetimes
$\mu_{n,p}$	electron and hole drift mobilities
$\mu_{n,p}^*$	electron and hole Hall mobilities
ω	angular frequency, $2\pi f$
∇	nabla operator

1. INTRODUCTION

Research in silicon magnetic field sensors over the last three decades seems to indicate that the magnetotransistors (MT) has the greatest application potential, primarily because of the high magnetic sensitivities [1,2] it has exhibited. Recent studies have also shown that MT's can be batch-fabricated in standard IC technologies such as bipolar or CMOS technology without design rule violations. The availability of low cost and high performance signal processing circuitry, particularly in bipolar IC technology, implies the attractive possibility of integrating the MT on the same die. An example of such an integrated MT is presented in [3], where the device replaces the input stage of an operational amplifier. A further attractive feature of MT's which distinguishes them from other silicon magnetic field sensors is their ability to detect several components of the magnetic field vector. By suitable modifications of the basic MT structure, two-dimensional [3] as well as three-dimensional [4] vector field detectors have been fabricated.

Offsets in magnetotransistors, unlike unipolar Hall plates, can unfortunately be quite high. Besides the geometrical imperfections introduced during the fabrication process, mechanical and thermal stresses resulting from the packaged die can also contribute to offsets. Offsets in devices fabricated in bipolar technology (< 111 > P-substrate) appear to be larger than their CMOS counterparts (< 100 > N-substrate). However, there are ways of reducing offset and they depend on the particular MT application (see [5]). The linearity of the MT's response is as good as for Hall plates in most cases [5]. One possible source of nonlinearity can be attributed to magnetoconcentration effects inherent in the device operation. Other possible sources of nonlinearity are offset variation with operating point and temperature, and variations of device parameters with temperature. With respect to noise, magnetotransistors have essentially the same characteristics as standard bipolar devices. However, by exploiting the inherent properties of noise (e.g., in multicollector structures), the output noise in MT's can be significantly reduced, thereby increasing the magnetic field resolution [6]. At low current operation ($I \leq 2$ mA), the temperature coefficient (TC) of MT's has been found to be as favourable as for Hall plates (see [5] and references therein).

As magnetic field sensors, MT's can be as effective as or superior to other silicon magnetic field sensors for switching and magnetometry applications. For example, the MT is useful in multidirectional magnetometry because of its vector direction capability. A pair of vertical MT's, integrated with peripheral circuitry have been designed [3] to detect the inplane vector field. Along the same lines, an omnidirectional magnetic switch can be integrated by combining "hysteresis" circuitry with the above configuration. Also, by integrating the MT with translinear circuits [7], a highly functional magnitude detector of three-dimensional fields can be realised.

In view of the above virtues, the MT deserves more scientific attention than it has received in the past, and an in-depth device analysis by both numerical simulation and measurements is worthwhile. The surprisingly wide range of magnetic sensitivities have intrigued researchers who continually devise new structures and propose intuitive analytical models such as Hall voltage or carrier deflection to explain their experimental findings. While some of these models remain valuable heuristic tools to explain MT operation in limiting cases, inconsistencies arise when a description of the underlying transport mechanisms for general device structures and operating conditions is attempted. Any such intuitive MT model has the character of an intelligent guess of the true solution of the carrier transport equations; i.e., the intuitive model is a hypothesis that ultimately has to be verified by solving the full transport equations (either analytically, or more likely numerically) with appropriate material (processing) parameters and boundary conditions. In favourable cases it may turn out that the carrier transport solutions yield potential, current, and carrier density distributions that can be interpreted in terms of the one or the other intuitive model. For example, the Hall voltage (electric potential gradient) and carrier (current) deflection have been verified to dominate the carrier transport pattern in very long, and very short extrinsic semiconductor slab geometries, respectively [5]. On the other hand, features of both potential gradient and current deflection were found to blend, in a quadratic (square) extrinsic semiconductor slab, which makes the two intuitive models obsolete in this case. In general, the applicability of intuitive models outside their proven validity limits, cannot be taken for

granted. In particular, the complex interaction of galvanomagnetic effects and bipolar action in the MT requires at least two-dimensional carrier transport analysis.

In order to check by experimental means, the true physical principles underlying the MT operation, novel test procedures have been devised which, besides the usual "black-box" output response, also facilitate direct measurement of the internal behaviour of certain physical quantities such as voltage [8]. Such procedures, however, yield the voltage distribution for only part of the device and are unable to detect the voltage at crucial areas (such as those in close proximity to the emitter base junction), due to the limitations imposed by present fabrication technology. Therefore, numerical modeling is still indispensable for determining the spatial distribution of various physical quantities such as electrostatic potential, current density, and carrier densities. Computations of a relatively high precision can be easily performed to prove or disprove the significance of certain physical effects [9].

In this work, an analysis of carrier transport is presented for magnetotransistors fabricated in standard CMOS and bipolar IC technologies. Results in terms of potential and current density distributions in the base region of MT's, have been obtained using numerical and novel experimental procedures. The experimental technique is based on a direct measurement of the Hall voltage in various MT structures that have minimum sized Hall probes placed at different parts of the base region. The voltage across the probes is monitored as a function of the operating point (injection level) and the magnetic field. The numerical results, which are based on high resolution computations ($\pm$ 0.5 μV stopping criterion), confirm the presence of a Hall field at the emitter base junction. But this Hall field is simply too weak in magnitude, for all practical injection levels, to cause any appreciable asymmetric emitter injection. The same pattern of behaviour is observed with the measured data. This asymmetric emitter injection effect has been widely used by researchers to explain the imbalance in the MT's collector currents, when subject to a magnetic field perpendicular to the injected curent. We thus rule out "emitter injection modulation" as a viable MT operating principle, in preference to carrier deflection for linear MT's. Possible nonlinearities in the MT's output response can be attributed to magnetoconcentration effects.

In the next section, a summary of previous MT analyses is presented. In particular, we critically review the Hall effect and its interaction with bipolar operation at the emitter base junction of the magnetotransistor. In Section 3, the approximations made and the crucial steps involved in the formulation of the galvanomagnetic transport equations are outlined. The formulation of the equations is pursued using the approaches adopted in formal transport theory as well as with the concepts of irreversible thermodynamics. This section also includes the system of model equations and boundary conditions underlying the numerical analysis. Unlike the usual $(B = 0)$ boundary conditions for the potential at the device's insulating boundaries, the boundary conditions in the presence of a magnetic field, have to be judiciously chosen so that the true Hall angle at the insulating boundaries is preserved. The procedure employed to deal with this problem is discussed. The various algorithms employed in the numerical procedure are presented in Section 4. The essential differences between the numerical procedures employed in this work and that of usual device modeling lie in the discretisation of the current continuity equations and in the treatment of the boundary conditions. A formal treatment of the discretisation procedure is provided. In Section 5, numerical as well as experimental results for a variety of device structures are illustrated. The numerical and experimental results are compared wherever appropriate and possible causes of discrepancy are discussed. Section 6 illustrates measurement results of $1/f$ noise in dual-collector MT structures fabricated in bipolar as well as CMOS technologies. In particular, we investigate the degree of correlation between the noise voltages of the collectors. Finally, the conclusions of both the theoretical as well as experimental findings are presented.

2. PREVIOUS MAGNETOTRANSISTOR ANALYSIS

As specific manifestations of the Lorentz force acting on moving charges (electrons and holes), three basic effects are usually assumed to be responsible for magnetic sensitivity in magnetotransistors: Hall effect, carrier deflection, and magnetoconcentration. These effects interact with the inherent bipolar action in a variety of ways. Depending on device geometry, fabrication process, and operating point, any one of these effects can prevail in favourable special cases. The effects are explained in the following sections but we focus mainly on the Hall effect and in particular, its interaction with bipolar operation at the emitter base junction. Detailed discussion of the other effects in the MT and the precise forms of the various analytical models, is beyond the scope of this work. However, a general form of the analytical models, particularly for carrier deflection is given. An elaborate account of the various effects and associated models can be found in [5,10].

2.1 Hall Effect

Analysis hitherto (see [5]), of the interaction of Hall fields and bipolar action in the base region of magnetotransistors, has led to the identification of three effects which possibly contribute to the imbalance of collector currents in dual-collector structures, viz.,

(i) asymmetric emitter injection - "emitter injection modulation",

(ii) contribution to minority carrier deflection by the Hall field generated by majority carriers - "indirect deflection",

(iii) modulation of the base transport factor.

The *emitter injection modulation* model was first proposed in [11], and has been subsequently invoked by several researchers to explain the output sensitivity of lateral and vertical magnetotransistors. Asymmetric emitter injection is believed to be caused by the buildup of a Hall voltage, $V_H(B)$ along the emitter base junction due to the action of Lorentz force on the injected minority and majority carriers. This supposedly leads to a modulation of the base emitter voltage, $V_{BE} \pm V_H(B)$ and consequently to a modulation of the collector

current, $I_C(B) \sim \exp\,[V_{BE} \pm V_H(B)]$. The resulting difference in collector currents, $[I_{C1}(B) - I_{C2}(B)]$, and subsequently the sensitivity for dual-collector structures

$$S = [I_{C1}(B) - I_{C2}(B)] \,/\, [(I_{C1} + I_{C2})\, B], \tag{2.1}$$

was then expressed as [11]

$$S = \sinh\,[V_H(B) \,/\, 2V_T] \,/\, B \tag{2.2}$$

where V_T denotes the thermal voltage, kT/q. The approach used in arriving at (2.2) was based on decoupling the P-N junction into two discrete Hall plates where neither of the plates include any portion of the space charge layer at the junction. Conventional Hall plate analysis is then employed to estimate the Hall fields in the respective plates. Depending on device geometry, doping and operating conditions, the analysis could lead to accurate estimates only in regions far away from the junction. The Hall fields resulting in these two regions are opposite in direction to each other and could in principle, be large. But at the space charge layer and, in particular, at the metallurgical junction, the distribution of charge is such that it resembles an "intrinsic" Hall plate with extremely small Hall coefficient and, hence, negligible Hall voltage. Depending on operating conditions, magnetoconcentration effects can possibly dominate at high injection by virtue of the Lorentz force acting on both electrons and holes. This would result in very little magnetic modulation of the net space charge at the junction. Hence, modulation of the electric potential by the magnetic field will be minimal, and this is basically due to the difference in Hall mobility of the electrons and holes. Consequently, the contribution of V_H to the total device sensitivity as expressed by (2.2), should be of no practical significance.

At this point, a clarification should be made of the misconception in the operating principle of the DAMS structure [12]. The DAMS is comprised of two vertical bipolar transistors in common-emitter configuration with the base region constituting a very large Hall plate. The sensitivity of the device (imbalance in collector currents) relies on the differential

emitter base voltage which is a consequence of the interaction of the Lorentz force and unipolar action. As in the usual Hall plate, the differential voltage is a function of the base Hall plate thickness, its resistivity, and of the base current. Hence, the DAMS structure does not rely on emitter injection modulation [5].

The emitter injection model was extended to fit experimental data obtained for single-collector [13] and dual-collector [14] lateral MT's fabricated in CMOS technology. In particular, the design geometry of the emitter in [14] was modified so as to yield a low emitter efficiency, and the Hall voltage supposedly obeys

$$V_H = R_H I B / t \tag{2.3}$$

where R_H is the Hall coefficient and t is some effective thickness. The fit to the measured data yielded a Hall voltage of 202 V/AT [14]. However, the design of low efficiency emitters using standard CMOS technology, does not affect the carrier densities and only leads to a reduction in the emitter current (because of the reduced injection area). Hence, there is no enhancement in the magnetic field modulation of minority carrier injection.

A similar approach was taken in [15,16] in fitting experimental data. The fit was made by linearising the sensitivity for small fields,

$$S \sim \exp(qV_H / nkT) \approx 1 + qV_H / nkT \tag{2.4}$$

and depending on the bias configuration, sensitivities of up to 300 /T obtained for their structure were attributed to the presence of a Hall voltage buildup across the base emitter junction. Unfortunately, a successful fit of the device sensitivity alone does not necessarily allow the conclusion of a unique operating model, because experiments do not provide complete access to the behaviour of potential and carrier densities in the device interior. Different potential and carrier density distribution patterns in the device may well yield similar output characteristics.

Indirect deflection refers to the contribution of the Hall field in the base region to the deflection of the minority carriers arriving at the collectors. As a result of the Lorentz force acting on the majority carriers, a Hall field is generated in the base region. The resultant

asymmetry in the electric field in the base region gives rise to further deflection of the minority carriers injected from the emitter. Just as in Hall plates, the Hall field in the base region is a function of the base resistivity, base geometry, and the base current. The Hall fields are large and favourable to deflection only when the base currents are sufficiently high but concurrently maintaining a low level of injection. This maximises the angle between the majority carrier current density and the resultant electric field in the base region. As the level of injection increases, the Hall fields deteriorate in magnitude because of the increased density of minority carriers which consequently yield a small Hall coefficient. At higher injection levels, the direction of the Hall field reverses and the boundary where this happens progressively moves with increasing injection levels. The models that describe the level of contribution of the Hall field to minority carrier deflection are described in Section 2.2.

The extent to which *modulation of the base transport factor* plays a role is determined by the magnitude of the Hall field that is generated by the majority carriers in the base region. The asymmetry in the resultant potential distribution, could lead to differential gradients in potential between the parts of the base region leading to the collectors. This consequently produces a differential current gain,which for dual-collector MT's operated in common-base configuration, results in $\partial I_{C1}/\partial I_E \neq \partial I_{C2}/\partial I_E$.

2.2 Carrier Deflection

Carrier deflection is inherent in all magnetotransistors and is usually the prevailing mechanism for all dual-collector lateral and vertical MT structures ([10,17]). It is characterised by a high degree of linearity in the MT's output response. The injected minority carriers, in the presence of a magnetic field perpendicular to the injection trajectory, are deflected and give rise to an imbalance in the collector current, $\Delta I_C(B)$. This imbalance is usually characterised by a relation of the form (see for example [10])

$$\Delta I_C(B) = k\,(L/W)\,\mu_{n,p}^{*}\,B\,I_C. \tag{2.5}$$

Here, L denotes an effective trajectory length and W is an effective width of minority carrier injection. The dimensionless factor, k is a geometric parameter that is generally obtained by fitting the measured value of $\Delta I_C(B)$ with assumed values of L, W, and electron and hole Hall mobilities, $\mu_{n,p}^*$. We note that relation (2.5) considers only the effect of the Lorentz force on the injected minority carriers. It does not account for the Hall field in the base region that is generated by majority carriers. Hence, the relation (2.5) is valid only for a limited range of values of base resistivity, base geometry, and base current. Depending on the structural configuration of the MT, the geometrical parameters in (2.5) could be a function of the operating point.

If the action of the Lorentz force on majority carriers in the base region becomes significant, the effects of the resulting Hall field are conveniently superimposed into (2.5), thus preserving the general form of representation for the current imbalance, viz.,

$$\Delta I_C(B) = k\,(L/W)\,\mu_{eff} B\, I_C. \tag{2.6}$$

Hence, the contribution to minority carrier deflection due to the presence of the majority carrier Hall field appears in the term, μ_{eff} which is a sum of the majority and minority carrier Hall mobilities,

$$\mu_{eff} = \mu_n^* + \mu_p^* \tag{2.7}$$

where $\mu_{n,p}^*$ are positive constants. The relations (2.5) to (2.7), may perhaps serve as useful design aids, but they contain too many parameters which can be conveniently fitted on an *ad hoc* basis. The relations in their present form leave very little room for extracting any conclusive details about the interactions taking place in the device interior. In particular, the role of parameters such as the base resistivity, the emitter and base currents, and the base geometry, on minority carrier deflection should be pursued to a greater scientific depth.

2.3 Magnetoconcentration

When the MT is operated at high injection, and in the presence of a magnetic field perpendicular to the direction of injected current, there is ambipolar diffusion creating large electron and hole concentrations on the same side of the base region. This leads to a magnetic field modulation of the base resistance due to the magnetoconcentration (MC) effect. In regions where there is a large buildup of mobile charge, we see a localised decrease in base resistance resulting in a clustering of the current density flow distribution. The reverse happens at the region where there is a localised increase of base resistance. Although there is redistribution of mobile charge in regions where MC effects prevail, there is no noticeable effect of the magnetic field on the net space charge $[p(B) - n(B)]$. Since the effects on the electric potential are determined by the space charge, the local distribution of potential remains practically unperturbed by the presence of B. This results in current flow lines which are perpendicular to the equipotential distribution, although it does not necessarily mean that the local Hall angle there is zero [see eqns. (3.24) and (3.25)].

The effects of MC in MT's become noticeable when the base width is comparable in length to, or larger than the diffusion length of minority and majority carriers. It is also required that the base region is quasi intrinsic ($p \approx n$), which is achieved by operating the MT at very high injection levels. Under such conditions, the dependence of the individual collector currents on the magnetic field turns out to be nonlinear [17]. Despite the nonlinearities in the single ended collector currents, the differential output signal, $\Delta I_C (B)$ could turn out to be linear with the applied field (by cancellation of the nonlinearities through subtraction).

3. MODEL EQUATIONS FOR MAGNETOTRANSISTOR SIMULATION

The partial differential equations governing carrier motion in silicon MFS are outlined. The equations are based on the classical drift-diffusion formulation. Although they are a result of many approximations [18], they nevertheless provide an adequate description of the various transport phenomena. The physical dimensions and operating conditions normally encountered in practical MFS justify these approximations. The derivation of the equations (particularly those describing the galvanomagnetic carrier transport) in [19] is exhaustive, so only the crucial steps are presented here.

3.1 Poisson's Equation and Continuity Equations

The fundamental system of equations that describe the various physical processes occuring in semiconductor devices in general, are usually given by the following macroscopic form [18]

$$\operatorname{div}(\varepsilon \boldsymbol{E}) = q\rho \tag{3.1}$$

$$\operatorname{div} \boldsymbol{J}_{nB} - q\partial n/\partial t = qR \tag{3.2}$$

$$\operatorname{div} \boldsymbol{J}_{pB} + q\partial p/\partial t = -qR. \tag{3.3}$$

Here, $\boldsymbol{E} = -\operatorname{grad} \psi$ denotes the electric field with ψ denoting the electric potential, ε is the material permittivity, ρ the space charge, q the elementary charge, $\boldsymbol{J}_{nB}$, $\boldsymbol{J}_{pB}$ are magnetic field dependent current densities, R is the net recombination rate, and n, p denote particle densities for electrons and holes respectively. We note that Poisson's eqn. (3.1) and the continuity eqns. (3.2) and (3.3) remain in the same form as for the zero magnetic field case [18]. The effect of the magnetic induction, $\boldsymbol{B}$ manifests itself in the current density relations. This is described in the following section.

3.2 Galvanomagnetic Transport Equations

The carrier transport equations are generally derived using the approaches adopted in

microscopic transport theory [19]. A general form of the equations can also be derived using the concepts of irreversible thermodynamics [20]. By casting the thermodynamic relations describing the system into a suitable form and using Onsager's relations, the functional dependence of the various kinetic coefficients on the local intensive variables (potential, temperature) as well as on external forces like the magnetic field can be easily made apparent. These coefficients can then be quantitatively calculated using the results of microscopic transport theory.

The general form of the electric and heat current density relations in an isotropic semiconductor, based on the solution of Boltzmann's transport equation using the relaxation time approximation, can be expressed as [19]

$$J_e = M_{00}\,\mathrm{grad}\,(E_f/q) + M_{10}\,\boldsymbol{B}\times\mathrm{grad}\,(E_f/q) + M_{20}\,\boldsymbol{B}\,\boldsymbol{B}\,.\,\mathrm{grad}\,(E_f/q)$$
$$+ M_{01}\,\mathrm{grad}\,(T)\,/\,T + M_{11}\,\boldsymbol{B}\times\mathrm{grad}\,(T)\,/\,T + M_{21}\,\boldsymbol{B}\,\boldsymbol{B}\,.\,\mathrm{grad}\,(T)\,/\,T$$

$$J_q = -\,M_{01}\,\mathrm{grad}\,(E_f/q) - M_{11}\,\boldsymbol{B}\times\mathrm{grad}\,(E_f/q) - M_{21}\,\boldsymbol{B}\,\boldsymbol{B}\,.\,\mathrm{grad}\,(E_f/q)$$
$$-\,M_{02}\,\mathrm{grad}\,(T)\,/\,T - M_{12}\,\boldsymbol{B}\times\mathrm{grad}\,(T)\,/\,T - M_{22}\,\boldsymbol{B}\,\boldsymbol{B}\,.\,\mathrm{grad}\,(T)\,/\,T. \qquad (3.4)$$

Here, E_f denotes the Fermi energy (or the electrochemical potential [19]), and T denotes the temperature. The equations are valid for small driving forces (gradient of potential or temperature) [19], and they describe the interactions of the electric current and heat flow in the material when subject to an external magnetic field. The coefficients, M_{ik} are tensors and in the presence of a magnetic field, they are functions of $\boldsymbol{B}$ (as will be seen later). They become scalars for zero field in isotropic semiconductor material.

Considering N-doped Si material and under the assumptions used in [18], eqns. (3.4) for the case of electrons read

$$J_{ne} = -\,(M_{00} + M_{10}\,\boldsymbol{B}\times\; + M_{20}\,\boldsymbol{B}\,\boldsymbol{B}\,.\,)\,\mathrm{grad}\,\varphi_n$$
$$+\,(M_{01} + M_{11}\,\boldsymbol{B}\times\; + M_{21}\,\boldsymbol{B}\,\boldsymbol{B}\,.\,)\,\mathrm{grad}\,(T)\,/\,T$$

$$J_{nq} = (M_{01} + M_{11}\,\boldsymbol{B}\times + M_{21}\,\boldsymbol{B}\,\boldsymbol{B}\,.\,)\ \mathrm{grad}\ \varphi_n$$

$$- (M_{02} + M_{12}\,\boldsymbol{B}\times + M_{22}\,\boldsymbol{B}\,\boldsymbol{B}\,.\,)\ \mathrm{grad}\ (T)\,/\,T. \qquad (3.5)$$

where φ_n denotes the Fermi potential for electrons.

Using the concepts of irreversible thermodynamics, the electric and heat current densities in (3.5) can be adequately described by the relation (see [20])

$$J_k = \sum_j L_{jk} F_j \qquad (3.6)$$

where L_{jk} are the kinetic coefficients and are functions of the local intensive parameters such as temperature and potential, as well as the magnetic induction. F_j denotes the *j*th driving force (or the affinity) such as potential gradient or temperature gradient, and J_k denotes the *k*th component of current density (or flux). In arriving at (3.6), it has been assumed that the affinities imposed on the system are small, i.e. the thermodynamic system deviates only slightly from equilibrium. In such a case, the quadratic and higher order terms in (3.6) have been neglected and the system obeys a linear Markoff process [20]. In such a process, Onsager's relations are valid and constitute a very powerful tool. The relations state a symmetry between the *j*th affinity and the *k*th flux (and vice versa) when the effects are measured in opposite magnetic fields, viz.,

$$L_{jk}(\boldsymbol{B}) = L_{kj}(-\boldsymbol{B}). \qquad (3.7)$$

With the choice of current densities J_{ne} and J_{nq} as the fluxes, and grad φ_n and $-$ grad $(T)/T$ as the associated components of affinities respectively, the transport equations for the electrons read

$$\begin{bmatrix} J_{ne} \\ J_{nq} \end{bmatrix} = \begin{bmatrix} N_{11} & N_{12} \\ N_{21} & N_{22} \end{bmatrix} \begin{bmatrix} \mathrm{grad}\ \varphi_n \\ -\,\mathrm{grad}\ (T)\,/\,T \end{bmatrix} \qquad (3.8)$$

with N_{ik} denoting the corresponding tensors of kinetic coefficients. It should be noted that the

magnetic field does not appear explicitly in the dynamical equations (3.8) as a driving force. This is to be expected since the magnetic field does not introduce energy to the system (or conversely it does not affect the rate of local entropy production). In the absence of the magnetic field, Onsager's relation reduces the scalars $N_{12} = N_{21}$.

To simplify the subsequent analysis, the following configuration shall be employed. Assume that the magnetic induction, $\boldsymbol{B} = (0, 0, B)$ and the applied potential and temperature gradients are in the x-direction. By virtue of the Lorentz force, components of potential and temperature gradients result in the y-direction. The components in the z-direction are assumed zero, maintaining consistency with the assumption of isotropic material. The terms in relation (3.8), are now expressed in Cartesian components

$$J_{ne} = [\, J_{ne}^{x} \quad J_{ne}^{y} \,]^{T} \qquad J_{nq} = [\, J_{nq}^{x} \quad J_{nq}^{y} \,]^{T}$$

$$\nabla\varphi_{n} = [\, \nabla_{x}\varphi_{n} \quad \nabla_{y}\varphi_{n} \,]^{T} \qquad \nabla T = [\, \nabla_{x} T \quad \nabla_{y} T \,]^{T}$$

where the superscript T denotes the transposed vector. In terms of the kinetic coefficients, L_{ik}:

$$N_{11} = \begin{bmatrix} L_{11} & L_{12} \\ L_{21} & L_{22} \end{bmatrix} \qquad N_{12} = \begin{bmatrix} L_{13} & L_{14} \\ L_{23} & L_{24} \end{bmatrix}$$

$$N_{21} = \begin{bmatrix} L_{31} & L_{32} \\ L_{41} & L_{42} \end{bmatrix} \qquad N_{22} = \begin{bmatrix} L_{33} & L_{34} \\ L_{43} & L_{44} \end{bmatrix}. \qquad (3.9)$$

Note that due to the presence of the magnetic field, the fluxes are now $J_{ne}^{x}, J_{ne}^{y}, J_{nq}^{x}, J_{nq}^{y}$, and the associated affinities are $\nabla_{x}\varphi_{n}$, $\nabla_{y}\varphi_{n}$, $(-1/T)\,\nabla_{x} T$, and $(-1/T)\,\nabla_{y} T$. As long as the rate of local entropy remains the same over the products of fluxes and affinities, the symmetry relations given by Onsager hold [19]. This reduces the tensors, N_{ik} to the form

$$N_{11} = \begin{bmatrix} L_{11} & L_{12} \\ -L_{12} & L_{11} \end{bmatrix} \qquad N_{12} = \begin{bmatrix} L_{13} & L_{14} \\ -L_{14} & L_{13} \end{bmatrix}$$

$$N_{21} = \begin{bmatrix} L_{13} & L_{14} \\ -L_{14} & L_{13} \end{bmatrix}, \qquad N_{22} = \begin{bmatrix} L_{33} & L_{34} \\ -L_{34} & L_{33} \end{bmatrix}. \tag{3.10}$$

Note that due to Onsager's theorem, the equality of N_{12} and N_{21} still remains. The tensors are simplified on the following basis. The coefficients L_{11}, L_{13}, L_{22}, L_{24}, L_{33}, and L_{34} are even functions of B because of Onsager's relations and consequently so is L_{31} (= L_{13}) and L_{42} (= L_{24}). Due to the assumption of isotropic crystal symmetry, we further obtain $L_{11} = L_{22}$ and $L_{33} = L_{44}$. The remaining coefficients, L_{12} and L_{21} are identified as odd functions of B by virtue of Onsager's theorem. Hence, the number of independent kinetic coefficients, L_{ik} have been reduced to six. From hereon, one could proceed with the analysis of the variety of thermomagnetic and thermoelectric effects and their descriptive coefficients. The effects include the absolute thermoelectric power, the isothermal and adiabatic electrical and heat conductivities, the isothermal and adiabatic Hall and Nernst effects, and the Ettingshausen and Leduc-Righi effects [20].

If the system is assumed to be isothermal and considering only the electric current density, the preceding system of equations (after a slight change of notation) become

$$\begin{bmatrix} J_{nB}{}^{x} \\ J_{nB}{}^{y} \end{bmatrix} = \begin{bmatrix} L_{11} & L_{12} \\ -L_{21} & L_{22} \end{bmatrix} \begin{bmatrix} \nabla_x \varphi_n \\ \nabla_y \varphi_n \end{bmatrix}. \tag{3.11}$$

Recasting the electric current density in relations (3.5) into a form compatible with (3.11), and under the same conditions as before, we obtain (after a similar change of notation)

$$\begin{bmatrix} J_{nB}{}^{x} \\ J_{nB}{}^{y} \end{bmatrix} = \begin{bmatrix} -M_{00} & M_{10}B \\ -M_{10}B & -M_{00} \end{bmatrix} \begin{bmatrix} \nabla_x \varphi_n \\ \nabla_y \varphi_n \end{bmatrix}. \tag{3.12}$$

The coefficients M_{i0} take the form (see [19])

$$M_{i0} = \alpha_1 \int_0^{\infty} (1 + s^2)^{-1} \alpha_2 \, \alpha_3^{i+1} \, dE \tag{3.13}$$

where $\alpha_1 = (-q/3\pi^2)(2m^*/\hbar^2)^{3/2}$, $\alpha_2 = E^{3/2}(\partial f_o/\partial E)$, $\alpha_3 = (e\tau/m^*)$, and s denotes $\alpha_3 B$. Here, m^* denotes the effective mass, $\hbar = h/2\pi$ (with h being the Planck constant), E denotes the energy, and $\tau = \tau(E)$ is the energy dependent relaxation time. Expanding $(1 + s^2)^{-1}$ in (3.13) as an infinite series in B, the M_{i0} can be reduced to

$$M_{i0} = \sum_{j=0}^{\infty} (-1)^j B^{2j} \alpha_1 \int_0^{\infty} \alpha_2 \, \alpha_3^{i+1+2j} \, dE. \tag{3.14}$$

Identifying the kinetic coefficients, L_{ik} in (3.11) with the M_{ik} in (3.12), the following relations can be established using (3.14), viz.,

$$L_{11} = -M_{00} = -\sum_{j=0}^{\infty} (-1)^j B^{2j} \alpha_1 \int_0^{\infty} \alpha_2 \, \alpha_3^{1+2j} \, dE \tag{3.15}$$

$$L_{12} = B\,M_{10} = B \sum_{j=0}^{\infty} (-1)^j B^{2j} \alpha_1 \int_0^{\infty} \alpha_2 \, \alpha_3^{2+2j} \, dE. \tag{3.16}$$

On evaluation of the integral in (3.14), M_{00} turns out to be the electrical conductivity, $\sigma_{no} = q\mu_n n$ for zero magnetic field where μ_n denotes the electron drift mobility. The integral is evaluated by assuming the classical Boltzmann distribution for the carrier density and the dependence of relaxation time on energy by a power law [19]. From (3.15) and (3.16), we note that L_{11} is an even function of B and L_{12} is an odd function of B. This is consistent with the conclusions drawn from eqn. (3.10) which were derived solely using the principles of irreversible thermodynamics. Hence, the kinetic coefficient, L_{11} which is the electrical conductivity, σ_n can be expanded in powers of B

$$L_{11} = \sum_{j=0}^{\infty} \sigma_{nj} B^{2j} \tag{3.17}$$

and with (3.15), the coefficients σ_{nj} are expressed as

$$\sigma_{nj} = (-1)^j \alpha_1 \int_0^{\infty} \alpha_2 \alpha_3^{1+2j} \, dE. \tag{3.18}$$

We can proceed to evaluate quantities such as the Hall coefficient, Hall mobility, and the Hall angle in terms of the kinetic coefficients, L_{ik} obtained from thermodynamics (macroscopic) and subsequently with the M_{ik} obtained through microscopic transport theory.

The Hall coefficient can be defined as (see [19,20])

$$R_H \equiv \nabla_y \varphi_n / (J_{nB}^{\,x} B). \tag{3.19}$$

With system (3.11), and on applying the boundary condition that the transverse current $J_{nB}^{\,y} = 0$, we obtain

$$R_H = L_{12} / [(L_{11}^2 + L_{12}^2) B]. \tag{3.20}$$

We observe from (3.20), that R_H is an even function of B. Substituting (3.15) and (3.16) into (3.20), the Hall coefficient becomes

$$R_H = M_{10} / (M_{00}^2 + B^2 M_{10}^2). \tag{3.21}$$

The Hall mobility for electrons, can be defined as the absolute value of the product of Hall constant and electrical conductivity, hence

$$\mu_n^* = |L_{11} L_{12} / [B (L_{11}^2 + L_{12}^2)]|, \tag{3.22}$$

which is again observed to be an even function of B. With the appropriate substitutions, it now reads

$$\mu_n^* = |-(M_{10}/M_{00}) / [1 + B^2 (M_{10}/M_{00})^2]|. \tag{3.23}$$

Finally, if we define the Hall angle as the angle between the resultant gradient of the Fermi potential and current density vector, we obtain

$$k \, \mathrm{tg}\, \theta = (J_{nB} \times \mathrm{grad}\, \varphi_n) \,/\, (J_{nB} \cdot \mathrm{grad}\, \varphi_n) \tag{3.24}$$

where k is a unit vector indicating the direction of $(J_{nB} \times \mathrm{grad}\, \varphi_n)$. Using (3.11), the right hand side of eqn. (3.24) can be evaluated and with appropriate substitutions, the Hall angle now reads

$$\mathrm{tg}\, \theta = L_{12} / L_{11} = - B\, (M_{10} / M_{00}). \tag{3.25}$$

If in (3.14), the integral is evaluated with a low field expansion in B, the resulting electric current density (3.12) in vector form reads [19]

$$J_{nB} = - \sigma_{no}\, \mathrm{grad}\, \varphi_n - \sigma_{no} A_1 \mu_n B \times \mathrm{grad}\, \varphi_n - \sigma_{no} A_2 \mu_n^2 B \times (B \times \mathrm{grad}\, \varphi_n) \tag{3.26}$$

where
$$A_i = [\Gamma(5/2)]^i \, \Gamma[5/2 + (i+1)r] \,/\, [\Gamma(5/2 + r)]^{i+1} \tag{3.27}$$

and $\Gamma(x)$ denotes the gamma function. The coefficients, A_i for $r = -1/2$ (phonon scattering) turn out to be $A_1 = 3\pi/8 = 1.18$ and $A_2 = 9\pi/16 = 1.77$. In the case of ionised impurity scattering ($r = 3/2$), $A_1 = 315\pi/512 = 1.93$ and $A_2 = 15\pi/8 = 5.89$. For neutral impurity scattering, $r = 0$ and we obtain $A_i = 1$. In general, A_i are statistical coefficients which depend on the nature of the scattering mechanism, the band structure, the degree of degeneracy, and on the statistics characterising the velocity distribution of carriers [21].

Taking the vector product of B with (3.26) and multiplying throughout by $A_1 \mu_n$, we obtain

$$A_1 \mu_n B \times J_{nB} = - \sigma_{no} A_1 \mu_n B \times \mathrm{grad}\, \varphi_n - \sigma_{no} A_1^2 \mu_n^2 B \times (B \times \mathrm{grad}\, \varphi_n). \tag{3.28}$$

In (3.28), the terms beyond those quadratic in B have been excluded. If we assume that $A_1^2 = A_2$, and substituting (3.28) into (3.26), the resulting magnetic field dependent current density can be elegantly represented in the form

$$J_{nB} + \mu_n^* J_{nB} \times B = - q\, \mu_n\, n\, \mathrm{grad}\, \varphi_n \tag{3.29}$$

where $\mu_n^* = A_1 \mu_n$ denotes the Hall mobility. Despite the differences between the theoretical values of A_1^2 and A_2, the errors involved in the assumption, $A_1^2 = A_2$ are trivial in the case of the weak field limit, $(\mu_n^* B)^2 << 1$, since the higher order terms in B in the M_{ik}'s become negligible. Furthermore, the measured values of A_i have been found to be significantly different from theory, particularly in the limit $r = 3/2$ (ionised impurity scattering) (see [10]). Considering the expression for the Hall mobility given by (3.23), it appears crude to approximate μ_n^* as being proportional to μ_n. But we note that this proportionality is indeed obtained for the case of low fields, as indicated by eqn. (3.23).

The equation for the magnetic current density for holes,

$$J_{pB} - \mu_p^* J_{pB} \times B = -q \, \mu_p p \operatorname{grad} \varphi_p \tag{3.30}$$

is analogously obtained. Here, μ_p^* denotes the Hall mobility for holes, μ_p the corresponding drift mobility, and φ_p the Fermi potential.

3.3 The Basic System

Under various assumptions (see [18]), the Fermi potentials in (3.29) and (3.30) can be expressed in terms of the electric potential and the carrier densities

$$\varphi_n = \psi - V_t \log_e (n/n_i)$$

$$\varphi_p = \psi + V_t \log_e (p/n_i) \tag{3.31}$$

where n_i denotes the intrinsic concentration and $V_t = kT/q$ denotes the thermal voltage. Substituting the above relations into (3.29) and (3.30), and using Einstein's relations

$$D_{n,p} = \mu_{n,p} \, kT/q \tag{3.32}$$

to define the diffusion constants $D_{n,p}$, the electric current densities in the presence of a magnetic field can be expressed as in the classical drift-diffusion formulation

$$J_{nB} + \mu_n^* J_{nB} \times B = qD_n [\text{grad } n - n \text{ grad } (q\psi/kT)] \tag{3.33}$$

$$J_{pB} - \mu_p^* J_{nB} \times B = -qD_p [\text{grad } p + p \text{ grad } (q\psi/kT)]. \tag{3.34}$$

In Poisson's equation (3.1), the space charge term ρ can be specified as [18], $\rho = q(p - n + N)$ with $N = N_D - N_A$ denoting the fully ionised net impurity distribution. Under steady state conditions, eqns. (3.1) to (3.3) reduce to the following system

$$\begin{aligned} &\text{div } (\varepsilon \text{ grad } \psi) = -q(p - n + N_D - N_A) \\ &\text{div } J_{nB} = qR \\ &\text{div } J_{pB} = -qR. \end{aligned} \tag{3.35}$$

System (3.35) with the transport relations (3.33) and (3.34), together with appropriate boundary conditions are sufficient to describe the transport phenomena in the device. The system is of macroscopic character and does not take into account any quantum effects. Quantum effects become important if the device feature sizes are in the order of the de Broglie wavelength of the particle [22].

The transport relations in the form described by (3.33) and (3.34) are a good approximation only in the weak field limit, $(\mu_{n,p}^* B)^2 << 1$. They take into account the direct effects of temperature on the various coefficients, but they do not include thermoelectric and thermomagnetic effects. The relative error due to the weak field approximation is of the order of $(\mu_{n,p}^* B)^2$.

3.4 Boundary and Interface Conditions

Equations (3.33) to (3.35) are solved subject to a mixture of Dirichlet and homogeneous Neumann boundary conditions. To ensure ohmic contacts, the contact regions have a sufficiently high dopant concentration and the contacts are assumed ideal. Hence, the electrostatic potential and carrier concentrations at the contact are prescribed by the usual Dirichlet boundary conditions [18]:

$$\psi = V_a + (kT/q)\sinh^{-1}(N/2n_i)$$
$$n = (N^2/4 + n_i^2)^{1/2} + N/2 \qquad (3.36)$$
$$p = (N^2/4 + n_i^2)^{1/2} - N/2$$

for an applied voltage, V_a at the contact.

The presence of a magnetic field could result in a significant Hall field at the device's insulating boundaries. In such a case, the standard condition grad $\psi \cdot \mathbf{s} = 0$ at these insulating boundaries may be physically invalid ($\mathbf{s}$ denotes the outward normal vector) and therefore, we adopt the procedure introduced in [23]. The actual boundary condition on ψ at these boundaries is treated as unknown and to deal with the problem we introduce an "artificial" oxide region that completely encloses the device domain. In this way, we avoid imposing artificial boundary conditions at the device/oxide interface which could *apriori* affect the results. The interface is assumed to be ideal (no interface traps) and the trapped charge density in the oxide region is assumed zero. The discontinuities in the normal component of electric field at the interface are handled in the weak formulation of the equations. Poisson's equation is solved over the entire domain (consisting of the device plus oxide), with the normal component of electric field taken to be zero at the oxide's outer edges. The nature of this condition might affect the solution in the device's active region. These effects, however, should be minimal, due to the chosen thickness of the oxide region.

In the oxide region, only Laplace's equation is solved since zero mobile and oxide trapped charge densities are assumed. The solutions of the continuity equations are restricted to within the device domain. At the semiconductor/oxide interface, the zero normal current condition ($J_n \cdot \mathbf{s} = J_p \cdot \mathbf{s} = 0$) is imposed.

3.5 Physical Models

We assume that the mobile charge is subject to purely lattice and impurity scattering, in which case the drift mobilities obey the model proposed by [24]

$$\mu_{n,p} = \mu_{n,p}^{min} + \frac{\mu_{n,p}^{L} - \mu_{n,p}^{min}}{1 + (N_T/N_{n,p}^{ref})^{\alpha_{n,p}}} \quad (3.37)$$

where the lattice mobilities, $\mu_{n,p}^{L}$ are 1330 cm^2/Vs and 495 cm^2/Vs for the electrons and holes respectively. The empirical coefficients, $\mu_{n,p}^{min}$ are 65 cm^2/Vs and 47 cm^2/Vs, $N_{n,p}^{ref}$ are 8.5×10^{16} cm^{-3} and 6.3×10^{16} cm^{-3}, $\alpha_{n,p}$ are 0.72 and 0.76, and N_T denotes the total impurity concentration, $N_D + N_A$. The Hall mobilities have been assumed proportional to the drift mobilities (see Section 3.2). In view of the scattering mechanisms we have assumed, and since we are dealing with weak fields, $A_{\dot{}}$ was chosen to be 1.2 for both electrons and holes.

The generation-recombination phenomena are assumed to be restricted to the processes related to the presence of trap centers. Based on the theory developed by Shockley-Read-Hall, the net recombination rate was modeled using (see [25])

$$R = (pn - n_i^2) / [\tau_p (n + n_o) + \tau_n (p + p_o)]. \quad (3.38)$$

Here, n_o and p_o are functions of the energy level of trap centres. This energy level is usually not known and following common practice (see [26]), it is assumed identical to that of the intrinsic Fermi level, in which case $n_o = p_o = n_i$. The intrinsic concentration, n_i is assumed uniform throughout the device. The respective electron and hole carrier lifetimes $\tau_{n,p}$ are assumed to be functions of the impurity doping concentration. According to the model proposed by Fossum (see [25])

$$\tau_{n,p} = \tau_{n,p}^{o} / (1 + N_T / N_{n,p}^{o}) \quad (3.39)$$

where $\tau_{n,p}^{o}$ are 3.95×10^{-4} s and 3.52×10^{-5} s, and $N_{n,p}^{o}$ identically equals 7.1×10^{15} cm^{-3}.

4. NUMERICAL PROCEDURE

The model equations shown in Section 3 are discretised on a triangular grid. A fine mesh is employed at appropriate locations to provide better resolution to the doping profile and to the nonlinear behavior of the electrostatic potential. The mesh generation/refinement procedure is based on a combination of the well known regular grid triangulation and Delauney triangulation [27] schemes. Due to the awkward structural nature of magnetotransistors (large junction aspect ratios), neither of the above procedures on their own was found to be efficient in optimising the total number of nodes generated. The regular grid triangulation scheme is economical on the total node count but fails to efficiently resolve curved regions. Delauney triangulation on the other hand provides a good resolution of nonrectangular regions, but has the drawback of generating an excessive number of nodes because of its inherent property to generate optimally shaped elements (equilateral triangles). In view of these drawbacks, a combination of both schemes is employed where the latter is used in the triangulation of curved regions (such as junction sidewalls) and the former everywhere else (see Fig. 4.1). Care was taken to ensure that all angles in an element were as large as possible in accordance to the standard error analysis [28]. The algorithms employed in the grid generator will be presented elsewhere.

4.1 DISCRETISATION SCHEME

The discretisation scheme employed is based on the control region approximation [29] or more commonly known as the box integration method (see [30]). This method when applied to any of the equations in system (3.35), transforms it by means of Gauss' divergence theorem into a system of discrete algebraic equations expressed as a function of the respective unknowns, ψ, n, and p. Details of the scheme are illustrated in the two subsections that follow.

4.1.1 Poisson's Equation

Following standard procedure, the continuous form of Poisson's equation in (3.35) is

first linearised by a Newtonian scheme around a known potential, ψ^o. For small deviations in potential, it reads

$$-div(\varepsilon \text{ grad } \psi) + (q/V_t)(p^o + n^o)\psi - (q/V_t)(p^o + n^o)\psi^o - \rho^o = 0 \quad (4.1)$$

where
$$p^o = n_i \exp[(\varphi_p{}^o - \psi^o)/V_t]$$
$$n^o = n_i \exp[(\psi^o - \varphi_n{}^o)/V_t]$$
$$\rho^o = p^o - n^o + N. \quad (4.2)$$

Applying the divergence theorem to eqn. (4.1) transforms it into a system of algebraic equations found by solving for any node i the equation:

$$-\int_{\partial\Omega_i} \varepsilon \text{ grad } \psi \,.\, \boldsymbol{s}\, d(\partial\Omega_i) + \int_{\Omega_i} (q/V_t)(p^o + n^o)\psi\, d\Omega_i$$
$$-\int_{\Omega_i} [(q/V_t)(p^o + n^o)\psi^o + \rho^o]\, d\Omega_i = 0 \quad (4.3)$$

where Ω_i is the cell (or subdomain) formed by the union of perpendicular bisectors of element edges that converge to node i (see Fig. 4.2), $\partial\Omega_i$ denotes the boundary of Ω_i and $\boldsymbol{s}$ the outward normal vector to $\partial\Omega_i$. The choice of perpendicular bisectors of element edges keeps calculations of flux emanating from node i, relatively simple. The electrostatic potential, ψ is assumed to be spatially linear within an element (i.e. the electric fields are piecewise constant in the domain). By assuming a piecewise constant material permittivity, ε the discretised form of eqn. (4.3) can easily be evaluated. For a chosen element, the discretised equation for node i reads

$$V_t\, \varepsilon\, [d_{ij} / \ell_{ij} (\psi_i - \psi_j) + d_{ik} / \ell_{ik} (\psi_i - \psi_k)] + \int_A (q/V_t)(p^o + n^o)\psi\, dA$$
$$-\int_A [(q/V_t)(p^o + n^o)\psi^o + \rho^o]\, dA = 0 \quad (4.4)$$

where the subscripts associated with d and ℓ denote scalar distances of the perpendicular bisectors and elemental edges respectively, and A denotes a portion of subdomain Ω_i that is encompassed by d_{ij} and d_{ik} (see Fig. 4.3). The charge density terms $(p^o + n^o)$ and ρ^o in eqn. (4.4) are assumed to be spatially linear functions within the element. The approximation of linearly varying charge density should lead to solutions of sufficient accuracy since a high density of mesh points has been employed at the edges of the depletion regions where nonlinearity in the potential is high. The integrals over A are evaluated by simple numerical integration using triangular area coordinates [31]. A more accurate technique of evaluating the nonlinear charge density integrals would be to employ an n-point Gauss quadrature. A sufficiently high accuracy could be achieved with a six point formula [32]. The procedure employed in obtaining eqn. (4.4) is then repeated on an element by element basis covering the entire simulation domain..The entries for the stiffness and right hand side matrices are updated in the process.

4.1.2 Carrier Continuity Equations

The discretisation of the electron and hole continuity equations is based on the two-dimensional extension (to triangular grids [33]) of the Scharfetter-Gummel approach [34] but with the asymmetries introduced by the magnetic field suitably incorporated. Due to these asymmetries, variations in the standard procedure were employed in determining the projected current density along the edge of an element under consideration. This involves taking into account all three nodal values of ψ, n, and p pertaining to the element.

In what follows, the steps leading to the discretised form for the electron continuity equation are presented. An analogous approach holds for that of holes. We recall that the magnetic field dependent electron current density (3.33) reads

$$J_{nB} + \mu_n^* J_{nB} \times B = J_{no} \tag{4.5}$$

where the right-hand side is the zero field current,

$$J_{no} = qD_n\,(\text{grad}\, n - n\, \text{grad}\,(\psi/V_t)]. \tag{4.6}$$

Expressing J_{no} in divergence form and projecting it onto an element side connected by nodes a and b yields

$$J_{no} \cdot u_{ab} \exp(-\psi/V_t) = qD_n\, \text{grad}\,[n \exp(-\psi/V_t)] \cdot u_{ab} \tag{4.7}$$

where u_{ab} denotes the unit vector parallel to the side. For the element under consideration (say element with vertices i, j, k shown in Fig. 4.3), the integrals of (4.7) along paths i to j and i to k yield

$$J_{no} \cdot u_{ij} = qD_n/\ell_{ij}\,[n_j B(\psi_{ji}/V_t) - n_i B(\psi_{ij}/V_t)],$$
$$J_{no} \cdot u_{ik} = qD_n/\ell_{ik}\,[n_k B(\psi_{ki}/V_t) - n_i B(\psi_{ik}/V_t)] \tag{4.8}$$

respectively. The left hand side of eqns. (4.8) denote scalar current densities and $n_{i,j,k}$ denote the respective nodal electron concentrations. To arrive at (4.8), the scalar current density, $J_{no} \cdot u_{ab}$ is assumed constant along the elemental edge, the mobility μ_n (and consequently D_n) is assumed constant in the element and is replaced by an average elemental value. The electric potential is as before assumed to be spatially linear. As in zero field cases, B denotes the Bernoulli function which is defined as $B(\Delta) = \Delta / [\exp(\Delta) - 1]$ where Δ denotes the potential difference between nodes, $\psi_{ab} = \psi_a - \psi_b$. We can extract the zero field current density, J_{no} in the element;

$$J_{no} = U^{-1} F_n \tag{4.9}$$

where

$$J_{no} = \begin{bmatrix} J_{no}^{x} \\ J_{no}^{y} \end{bmatrix} \qquad U = \begin{bmatrix} U_{ij}^{x} & U_{ij}^{y} \\ U_{ik}^{x} & U_{ik}^{y} \end{bmatrix}$$

and

$$F_n = \begin{bmatrix} qD_n/\ell_{ij}\,[n_j B(\psi_{ji}/V_t) - n_i B(\psi_{ij}/V_t)] \\ qD_n/\ell_{ik}\,[n_k B(\psi_{ki}/V_t) - n_i B(\psi_{ik}/V_t)] \end{bmatrix}. \tag{4.10}$$

Returning to eqn. (4.5), the magnetic field current density J_{nB} in terms of its components, can be expressed as

$$\beta_n J_{nB} = J_{no} \tag{4.11}$$

where

$$\beta_n = \begin{bmatrix} 1 & \mu_n^* B \\ -\mu_n^* B & 1 \end{bmatrix}. \tag{4.12}$$

Substituting for the zero field current (4.9) into (4.11), the magnetic field current density can now be fully determined, viz.,

$$J_{nB} = \beta_n^{-1} U^{-1} F_n. \tag{4.13}$$

Having constructed the magnetic field current density J_{nB} in the element, the standard procedure is now employed in obtaining the discretised form of the electron continuity equation. By assuming J_{nB} is constant in the element, the flux or the current emanating from node i is evaluated in the usual manner. With an arithmetic average of the Hall mobility, μ_n^* and with the usual assumption that the electric field is piecewise constant, the divergence theorem is applied to the continuity equation in system (3.35). For a subdomain, Ω_i this yields,

$$\int_{\Omega_i} \mathrm{div}\, J_{nB}\, d\Omega_i = \int_{\partial\Omega_i} J_{nB} \cdot \mathbf{s}\, d(\partial\Omega_i) = \int_{\Omega_i} qR\, d\Omega_i \tag{4.14}$$

where the integral over $\partial\Omega_i$ denotes the flux related to node i. In the element under consideration, the contribution of flux to node i from its neighbours, j and k can be expressed in the form

$$J_{nB}^T U^T D = F_n^T [U^{-1}]^T [\beta_n^{-1}]^T U^T D \tag{4.15}$$

where $D = [d_{ij} \;\; d_{ik}]^T$. The discretised form of the electron continuity equation reads

$$F_n^T [U^{-1}]^T [\beta_n^{-1}]^T U^T D = qA\,(n_i p_i - n_{ii}^2)/[\tau_p (n_i + n_o) + \tau_n (p_i + p_o)]. \tag{4.16}$$

where n_i, p_i, and n_{ii} denote the electron, hole, and Intrinsic concentrations respectively at node i and $\tau_{n,p}$ denote the electron and hole lifetimes. The right hand side of eqn. (4.14) is evaluated by assuming a constant net recombination in A. Again a more accurate treatment of the recombination integral in eqn. (4.14) can be performed by employing an n-point Gauss quadrature formula [32].

An analogous treatment yields the discretised form for the hole continuity equation;

$$F_p^T [U^{-1}]^T [\beta_p^{-1}]^T U^T D = -qA\,(n_i p_i - n_{ii}^2)/[\tau_p (n_i + n_o) + \tau_n (p_i + p_o)] \qquad (4.17)$$

where

$$F_p = \begin{bmatrix} -qD_p/\ell_{ij}\,[p_j B(\psi_{ij}/V_t) - p_i B(\psi_{ji}/V_t)] \\ \cdot \\ -qD_p/\ell_{ik}\,[p_k B(\psi_{ik}/V_t) - p_i B(\psi_{ki}/V_t)] \end{bmatrix}$$

and

$$\beta_p = \begin{bmatrix} 1 & -\mu_p^* B \\ \cdot & \\ \mu_p^* B & 1 \end{bmatrix}. \qquad (4.18)$$

The entries to the stiffness matrix are assembled on an element by element basis, skipping those elements in the oxide region. This way, the solution to the continuity equations is restricted to within the device domain with the no-flow current density condition at the device/oxide interface naturally recovered. In eqns. (4.16) and (4.17), the presence of the terms $[U^{-1}]^T [\beta_{n,p}^{-1}]^T U^T$ results in a stiffness matrix that is positive definite nonsymmetric due to the magnetic field ($\mu_{n,p}^* B \neq 0$) which explicitly shows up in $\beta_{n,p}$. This represents the difference between this work and the usual cases of $B = 0$ that is widely found in the literature (see [18]). Indeed for zero fields ($\mu_{n,p}^* B = 0$), $[U^{-1}]^T [\beta_{n,p}^{-1}]^T U^T$ results in an identity matrix. Hence, the flux contribution to node i (for the case of electrons) simply reduces to

$$F_n^T D = qA\,(n_i p_i - n_{ii}^2) / [\tau_p (n_i + n_o) + \tau_n (p_i + p_o)] \qquad (4.19)$$

resulting in a positive definite symmetric stiffness matrix. Expression (4.19) is identical to the

formulations employed in numerical device analysis using the box integration method.

4.2 SOLUTION SCHEME

The discretised equations discussed in the previous section are solved by using a nonlinear procedure which employs basically a successive scheme (Gummel's algorithm, see [35]). The solution procedure is initiated by solving the nonlinear Poisson's equation (inner loop), with the quasi Fermi potentials kept constant. The nonlinear procedure employs an acceleration algorithm where the update for the potential is damped,

$$t\,\delta u = \psi^{k+1} - \psi^{k} \tag{4.20}$$

with the damping parameter, t evaluated along the lines suggested by [36]. A facility is provided in the code whereby the acceleration algorithm can be invoked or disabled if so desired, at any stage in the iterative process, based on the residues which are continuously monitored. The acceleration algorithm appears efficient only with good trial values of the potentials. With bad trial values, invoking the accelerator has often led to residues which successively increase after every iteration in the inner loop ultimately leading to divergence. If the residues after the first few iterations are observed to be monotonically decreasing, the acceleration is invoked at every subsequent iterative step. This appears to substantially reduce the number of iterations required for the convergence of the electric potential in the inner loop. When the inner loop iterations have been satisfactorily terminated, the concentrations n and p are updated with the new value of ψ which is in turn kept constant during the subsequent solution of the continuity equations.

An iterative process is employed in the solution of continuity equations to yield self consistent values of n and p for the given ψ. At each iteration step, the recombination terms on the right hand side of the continuity equation are evaluated with the most recent updates of n and p. We found that this procedure reduced the total number of outer loop iterations necessary for the complete convergence of ψ, n, and p.

To obtain solutions of the variables for a desired device operating point, the applied

bias is incremented in steps starting from the zero bias (or equilibrium) solution. The trial values for the potentials at zero bias are obtained by assuming space charge neutrality and thermodynamic equilibrium of the charged carriers. Typical increments in bias voltage were around 0.2 V at low injection and 0.1 V at high injection. At the first bias increment a careful extrapolation of the electrostatic potential is made, based on an assumed behaviour of quasi Fermi potentials at the N and P regions. At the next increment in applied bias, the trial values for the potentials are constructed from a linear interpolation of the previous two iterates. This way, no convergence difficulties were encountered in simulations leading up to an applied potential of 0.9 V. Problems however were encountered at higher injection levels particularly with the solution to the continuity equations, primarily due to the strong coupling of ψ, n, and p through the recombination terms. Such convergence difficulties encountered with the decoupled scheme could be alleviated with the partial linearisation of the recombination terms in the continuity equations as shown in [37]. This is shown in Appendix 1 for the case of magnetic transport equations.

An improved guessing procedure for the solution variables could be achieved by linearising equations (3.33) to (3.35) around the solutions obtained for the preceding bias point. The solutions to the resulting linear equations serve as trial values for the subsequent bias point. This scheme is illustrated in Appendix 2.

The discretised equations are solved by a family of direct methods using SPARSPAK [38]. While this solver was found to give very good results, the storage requirements that were encountered in the simulation of various magnetic field sensitive bipolar devices, indicate that an iterative scheme such as the generalised conjugate gradient method would be far more preferable.

Although the variables in the system are ψ, n, and p, convergence checks are applied to the potentials: ψ, φ_n, and φ_p. The quasi-Fermi potentials are updated at the end of each continuity equation solution using relations (4.2). The convergence criteria for each node are as follows

$$(u^{k+1} - u^k) / u^{k+1} < \gamma_1 \qquad \text{for } u^{k+1} \geq 1.0$$
$$\text{and} \qquad (u^{k+1} - u^k) < \gamma_2 \qquad \text{for } u^{k+1} < 1.0 \tag{4.21}$$

where u represents the electric or quasi-Fermi potentials. The precise values of γ_1 and γ_2 are chosen depending on the problem at hand. To avoid unnecessary calculations, $\gamma_1 = \gamma_2 = 10^{-3}$ was found to be sufficient for the evaluation of device characteristics. In other situations, where the simulation is aimed at investigating the magnitude of certain physical effects imposed by the magnetic field (such as the Hall voltage in magnetotransistor structures [39]), γ_1 and γ_2 are typically in the order of 10^{-6}. The convergence criteria for the electric potential in the inner loop obeys (4.21) but with γ_1 and γ_2 an order of magnitude smaller.

4.3 Evaluation of Terminal Currents

Terminal currents are evaluated once the desired solution to the variables has been achieved, i.e. as a post processing step. A common feature in most magnetic field sensitive devices is the presence of multi-electrodes where the current imbalance between a pair of electrodes (such as collectors or drains) serves as a measure of the magnitude and direction of the magnetic field. Hence it is desirable to perform an accurate computation of the terminal current to determine true estimates of the device sensitivity to the field.

A well known technique of calculating a terminal current is by integrating the flux crossing the border of the contact and the device. Since the total current density involves numerical derivatives of the solution variables, large errors may result particularly at the union of Dirichlet and Neumann boundary conditions. Although the solutions to the variables are smooth at these regions, there may be singularities in the derivatives which yield singularities in the current density.

The technique outlined below employs an alternative approach to terminal current evaluation. This procedure appears to provide excellent conservation of terminal currents and

its implementation is straightforward in terms of computational complexity. Considering just the electrons for simplicity, the continuity equation can be represented in the weak form, viz.,

$$\int_{\Omega} \zeta \operatorname{div} J_{nB}\, d\Omega = \int_{\Omega} \zeta qR\, d\Omega \tag{4.22}$$

where ζ is a smooth test function and Ω represents the device domain. Equation (4.22) can be expressed as

$$\int_{\partial\Omega} (\zeta J_{nB}) \cdot \boldsymbol{s}\, d(\partial\Omega) = \int_{\Omega} J_{nB} \cdot \operatorname{grad} \zeta\, d\Omega + \int_{\Omega} \zeta qR\, d\Omega \tag{4.23}$$

where $\boldsymbol{s}$ is an outward normal vector and $\partial\Omega$ represents the device boundary. If ζ is chosen to be 1 over electrode α and zero at all other electrodes, the outward electron current at electrode α is then given by

$$I_{n\alpha} = \int_{\Omega} J_{nB} \cdot \operatorname{grad} \zeta\, d\Omega + \int_{\Omega} \zeta qR\, d\Omega. \tag{4.24}$$

Hence, the total current $I_{T\alpha}$ through electrode α is obtained by

$$I_{T\alpha} = I_{n\alpha} + I_{p\alpha} = \int_{\Omega} (J_{nB} + J_{pB}) \cdot \operatorname{grad} \zeta\, d\Omega. \tag{4.25}$$

An elegant test for the conservation of total electron device current can be performed by setting the test function ζ to be 1 over the entire device domain. This reduces (4.23) to

$$\int_{\partial\Omega} J_{nB} \cdot \boldsymbol{s}\, d(\partial\Omega) = I_{nL} = \int_{\Omega} qR\, d\Omega \tag{4.26}$$

where I_{nL} denotes the total electron leakage current. The right hand side integral in (4.26) can be conveniently evaluated since it only requires summing the various recombination integrals which have been performed earlier for each cell as seen by eqn. (4.16). The procedure employed in the test for conservation of hole current is analogous.

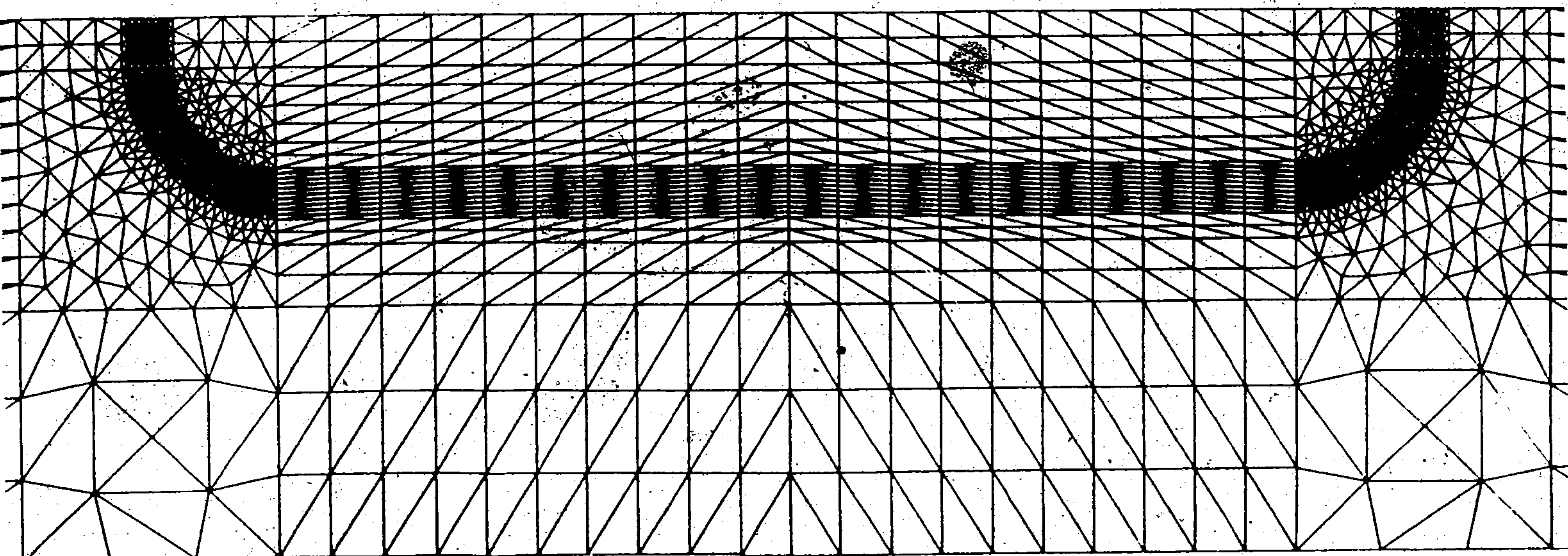

Fig. 4.1 Triangular mesh for an emitter base junction of a magnetotransistor, generated using Delauney triangulation at junction sidewalls and regular grid triangulation everywhere else.

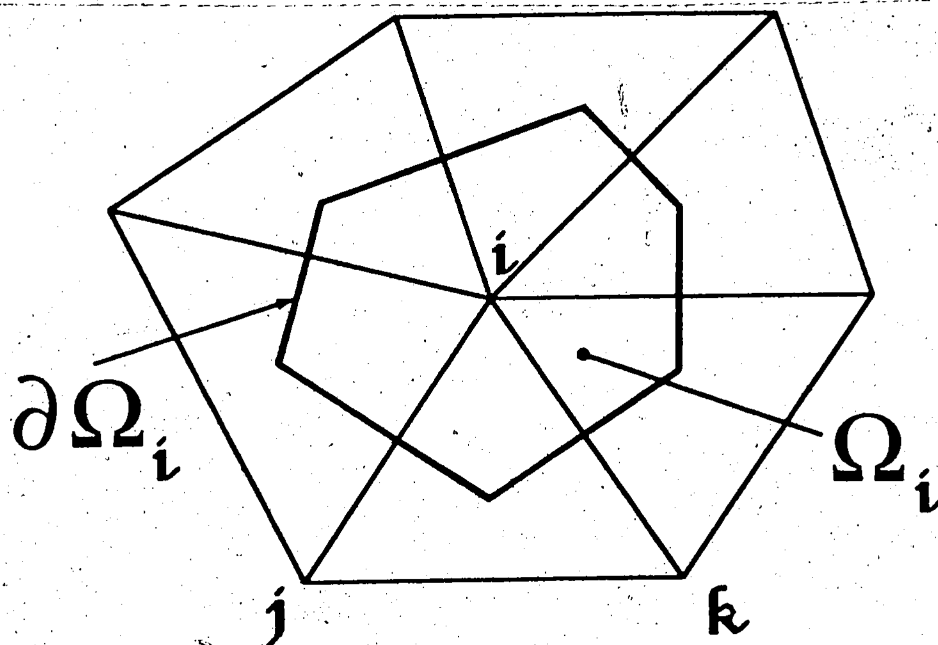

Fig. 4.2 The cell or subdomain, Ω_i (bounded by $\partial\Omega_i$) formed by the union of perpendicular bisectors of elemental edges converging to node i.

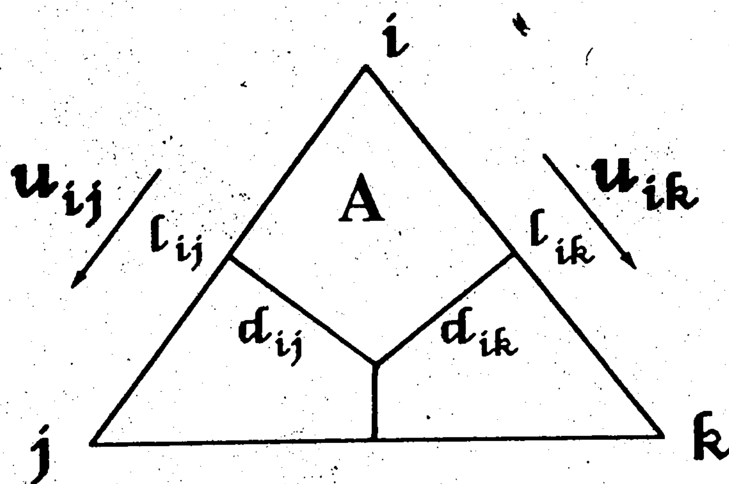

Fig. 4.3 An element with vertices i, j, and k, constituting part of the cell shown in Fig. 4.2. The notation used is described in the text.

5. GALVANOMAGNETIC CARRIER TRANSPORT ANALYSIS

Analysis of bipolar carrier transport, based on results of numerical simulations as well as measurements, is performed for a variety of device structures. The results of simulations, comprising of potential and current density distributions, allows one to investigate the significance of the basic physical mechanisms in the MT (such as Hall effect, carrier deflection, and magnetoconcentration), for various operating conditions. Pertinent measurement results obtained through novel experimental procedures seem to be in support of the conclusions drawn from the simulations. The numerical and experimental results are compared wherever appropriate, and possible causes of discrepancy are explained.

5.1 Simulation Results for Emitter Base Junctions

The analysis begins with a simulation of transport phenomena in a lateral P-N junction diode in the presence of a magnetic field perpendicular to the device surface [9,40]. The reason for choosing such a simple structure is to investigate very closely the behaviour of electrostatic potential at the junction vicinity, of a forward biased emitter base junction for different injection levels. The two-dimensional device geometry considered for the analysis is shown in Fig. 5.1. The device has a 10 μm base contact, 6 μm emitter contact, and a base width of 6 μm. An artificial oxide region that completely encloses the device has been introduced to deal with the problem of boundary conditions for the electric potential as discussed in Section 3.4.

The impurity distribution used in the simulations is as follows. The device has a uniform P-substrate with $N_A = 10^{16}$ cm^{-3}. At the base and emitter contact regions, the peak doping concentration is $N_A = 10^{20}$ cm^{-3} and $N_D = 10^{20}$ cm^{-3} respectively. N_A and N_D drop exponentially to a junction depth of $x_j = 1.3$ μm.

Figure 5.2 shows the distribution of electrostatic potential in the device as well as oxide regions for an applied bias of $V_{BE} = 1$ V and a magnetic field, $B = 2$ Tesla. There is no indication of any Hall field at the junction vicinity (Fig. 5.2), but a skew in the current density flow lines

is observed (Fig. 5.3) indicating the presence of carrier deflection. The skew is particularly noticeable for the minority carriers, due to the higher Hall mobility of the electrons. There also seems to be a weak clustering of the current densities, J_{nB} and J_{pB} to the same side of the base region. This is because of the build up of both carriers (see Fig. 5.4), leading to a localised region of higher conductance. The reverse happens on the other side of the base region where there is a localised region of higher base resistance [40].

The results shown above are from numerical computations that are based on a convergence criteria (4.21), γ_2 of 10^{-3} for the potentials in the outer loop. Increasing the resolution of the computations ($\gamma_2 = 10^{-6}$), simulations were performed for a diode structure [9] (Fig. 5.5) that is almost similar to the one previously discussed (Fig. 5.1). A magnetic field of B = 2 T is applied perpendicular to the diode surface.

At low injection ($V_{BE} = 0.7$ V), due to the rather low minority and majority current densities, we do not observe any effect of B on the potential. At high injection ($V_{BE} = 0.9$ V), there is a Hall field in the vicinity of the junction (AA') and its direction reverses in the neutral base region (BB'). This is illustrated in Fig. 5.6 where AA' and BB' in the figure denote cut lines at the emitter base junction ($x = 6.75$ μm) and neutral base region ($x = 5$ μm), respectively. The change in direction occurs in the range 6.4 μm $< x <$ 5.9 μm for $V_{BE} = 0.9$ V. The Hall voltage at the extremities of the junction (AA') turns out to be approximately 50 μV/T.

No magnetoconcentration (MC) effects occur at low injection since $n << p$. At medium and high injection levels, the relative concentration imbalance, $\Delta n/n_o = \Delta p/p_o$ across the device is about 0.01 /Tesla (see Fig. 5.7). Here, n_o and p_o denote the zero-field concentrations. The degree to which this MC effect contributes to MT sensitivity depends on base geometry and operating point (V_{BE} and V_{CE}).

5.2 Simulation Results [illegible]ctor Magnetotransistors

The structure considered for analysis is a lateral CMOS NPN dual-collector MT structure that is sensitive to magnetic fields perpendicular to the chip surface [23]. The two-dimensional geometry of the MT is shown in Fig. 5.8. The results of simulation for $V_{BE} = V_{CE} = 0.9$ V are illustrated in Figs. 5.9 - 5.11. These results are based on computations performed for a convergence criteria (4.21) of $\gamma_2 = 10^{-3}$ for the potentials in the outer loop.

The electrostatic potential and current density in the device at $B = 0$ are shown in Figs. 5.9 and 5.10 respectively. As expected, there is symmetry in the distributions. In the presence of a magnetic field, $B = 2$ T, the symmetry in the potential distribution at the emitter base junction appears to be still preserved, showing no sign of a Hall voltage buildup (see Fig. 5.11). However, the paths of both majority and minority carriers are observed to be skewed (Fig. 5.11). The asymmetry in the minority carriers (electrons) arriving at the collectors gives rise to an imbalance in the collector currents. The presence of magnetoconcentration effects in the device seems to be weak. The relative imbalance in the concentration is much less than that observed in the diodes that were analysed in the previous section. For the dual-collector MT structure considered, the dominating mechanism responsible for sensor action seems to be carrier deflection [23].

5.3 Measurement of Hall Voltage at Emitter Base Junction

The experiment is aimed to provide an indication of the Hall voltage at the emitter base junction of the recently devised highly sensitive suppressed sidewall injection magnetotransistor (SSIMT) [1]. The device is a dual-collector structure and fabricated using standard CMOS technology. It is sensitive to fields parallel to the chip surface, and has been reported to exhibit magnetic sensitivities (relative imbalance in collector currents) of 3 %/mT. The relative nonlinearity in the output sensitivity is less than 1 %/T. The device has a pair of P+ stripes adjacent to the N+ emitter. The function of the stripes is to suppress any sidewall drift and diffusion based minority carrier injection with appropriate stripe-emitter reverse

bias voltages. This feature seems to be crucial in enhancing the device's sensitivity to the field.

The experimental arrangement for this preliminary measurement of Hall voltage is shown in Fig. 5.12. The P+ stripes are biased with constant current sources, $I_{B1} = I_{B2} = I_E / 2$ to forward bias the emitter base junction. The differential voltage, V_D across the extremities of the junction is then monitored as a function of the magnetic induction applied parallel to the chip surface [9]. The SSIMT samples are mounted on suitable heat conducting nonmagnetic substrates and a uniform magnetic field is generated by a VARIAN V - 4005 four inch electromagnet which is operated by a VARIAN V - 2900 regulated power supply. The magnetic field is monitored by an LDJ - 511 Gaussmeter which employs an axial InSb Hall probe [41]. The samples are operated using an HP - 4145A semiconductor parameter analyser and the Hall voltage is measured using an HP 3478A multimeter which has a 100 nV resolution. The input impedance of the multimeter is greater than $10^{10}\ \Omega$ and the presence of the meter has no observable effect on the base currents flowing into the P+ stripes.

The differential voltage measured for various base currents is shown in Fig. 5.13 for a magnetic induction, $|B| \leq 0.9$ T. The observed sensitivity (V_D/AT) turns out to be around 1 V/AT at low currents [9] and decreases at larger operating currents. Using the Hall voltage model developed in [14], the sensitivity for the above geometry at $I_E = 1$ mA is calculated to be 15 V/AT which is an order of magnitude larger than the measured value. In the calculations, the Hall scattering coefficient, (μ_n^* / μ_n) was assumed to be 1.2, the substrate doping, $N_A = 10^{16}$ cm^{-3}, and the device thickness, t (emitter width in the direction of B) is 50 μm.

Although the above results are based on MT samples whose designs are not optimised for purposes of Hall voltage measurements, they nevertheless support the claims that were drawn from the numerical computations. A more accurate measurement technique using MT samples specifically designed for Hall voltage measurements [8] is discussed in the section that follows.

5.4 Experimental Results for MT in Common-Base Configuration

A variety of MT samples, fabricated in standard bipolar technology, were designed to facilitate a direct measurement of any Hall voltage buildup in the base region, including the areas that are in close proximity to the emitter base junction. This was achieved by a symmetrical placement of a pair of Hall probes in the base region. The samples were identical in geometry but of varying probe distances from the emitter base junction, i.e. $W' = 40$ µm, 60 µm, and 80 µm. In Fig. 5.14, the (a) top view and (b) cross-sectional view of the basic MT geometry is illustrated. The Hall probes have dimensions of 8 µm × 8 µm. These dimensions were a consequence of the minimum size offered by the design rules. Although the size restriction of the probes does not correspond to an ideal Hall voltage measurement, we nevertheless expect that due to the minute relative dimensions of the probe compared to those of the base region (140 µm × 80 µm), the internal potential distribution is not significantly perturbed by the presence of the pair of these localised equipotential surfaces [39].

The fabrication process for the samples considered is as follows. Starting from an epitaxially grown phosphorus doped N layer on a P-substrate (for the standard 44 V device), the boron doped P+ isolation regions are then formed. Next the P-base region is formed with boron diffusion followed by a phosphorus diffusion for the N+ collectors and emitter. Contact holes (including those for the Hall probes) are then cut and followed by the Al metallization process. The impurity concentration at a slice through the emitter base region at $x = 0$ is shown in Fig. 5.15. The profile was obtained by using the spreading resistance method. The junction depth, x_j is 2.5 µm and the other depths are as shown in Fig. 5.14.

The samples are mounted on nonmagnetic ceramic packages. The measurement apparatus used is described in the previous section. The current voltage characteristics obtained with the semiconductor parameter analyser for the MT operated in common-base configuration are given in Fig. 5.16 for emitter currents in 200 µA steps for a range of $0 \geq I_E \geq -1.2$ mA. The characteristics $I_{C1}, I_{C2} = f(I_E, V_{CB})$ have a scatter of less than 1% for the

MT's with the different Hall probe configurations. The variation in collector current offsets $\Delta I_C = (I_{C1} - I_{C2})$ in the various samples was less than 5%. The collector current imbalance, ΔI_C as a function of the magnetic field is shown in Fig. 5.17. The device is operated in the forward active mode in common-base configuration, $V_{CB} = 5$ V and $I_E = -1$ mA. The measured sensitivity, $S = \Delta I_C/(I_C B)$ is approximately 0.8 %/T with a relative nonlinearity of less than 1% for $|B| \leq 200$ mT.

The Hall voltage measurement for the various parts of the base region ($W' = 40$ µm, 60 µm, and 80 µm) is shown in Figs. 5.18 and 5.19 for $V_{CB} = 5$ V and $I_E = -1$ mA. At zero magnetic induction, the measured voltages correspond to the probe offsets. At reasonably close proximity to the emitter base junction ($W' = 40$ µm), the Hall voltage turns out to be around 20 µV/T for $|B| \leq 200$ mT (see Fig. 5.18), or 20 mV/AT in view of the 1 mA emitter current As the distance from the junction increases, the Hall voltage progressively drops and this can be observed from Fig. 5.19 where at $W' = 60$ µm and 80 µm, the measured voltages are 15 µV/T and 9.5 µV/T, respectively. We note that the direction of the Hall field (see Figs. 5.18 and 5.19) pertains to that of minority carriers (electrons). In the common-base configuration, this direction of Hall field at the base surface seems to be a function of the collector base voltage. The same behaviour, however, is not observed when the device is operated in common-emitter configuration. The collector currents are unaffected by the presence of the multimeter across the Hall probes.

The measurement results described above indicate that the Hall effect around the emitter base junction vicinity is much too small in magnitude (in the order of µV) to cause asymmetric emitter injection. This is in contrast to previous predictions [11] where the imbalance in collector currents was attributed to the presence of Hall fields along the emitter base junction [see relation (2.2)]. Rewriting relation (2.2) as

$$|V_H| = 2\, V_T \sinh^{-1} (\,|\Delta I_C / I|\,), \tag{5.1}$$

and using Fig. 5.17, the Hall voltage is calculated for the measured values of ΔI_C for $I = I_E = -1$ mA and with the zero field offsets nulled (Fig. 5.20). The predicted Hall voltage, although small in magnitude, is an order of magnitude larger than the Hall voltage measured across the probes (for $W' = 40$ μm). The analytical model [11] predicts 215 mV/AT as opposed to the measured value of 20 mV/AT obtained from Fig. 5.18. We note that the discrepancies between the predictions of the analytical model and measured results broaden, for MT structures of higher sensitivity, $|\Delta I_C / I_C| >> 0.1$.

5.5 Numerical and Experimental Results for MT in Common-Emitter Diode Configuration

Numerical simulations and experimental data of Hall voltage in the base region for the various MT samples are compared for different base emitter voltages. The MT is operated in the common-emitter configuration but with the collectors left to float. This essentially reduced device operation to that of a forward biased diode. The magnetic field as before is applied parallel to the chip surface.

5.5.1 Discussion of Numerical Results

The two-dimensional simulation domain is shown in Fig. 5.21. The oxide region (which completely encloses the device domain) is introduced for reasons discussed in Section 3.4. The oxide thickness is 1 μm on the device surface (consistent with the field oxide specifications of the technology) while on the device side and bottom walls an "artificial" oxide of 5 μm thickness replaces the base collector P-N junction [39].

The impurity distribution used in the simulations is as follows (see Fig. 5.15). In the base region, the peak acceptor concentration is 5×10^{17} cm^{-3} and follows a Gaussian

wall is 1.6×10^{16} cm^{-3}. At the emitter region, the peak donor concentration is 6×10^{19} cm^{-3} and the distribution is based on an exponential function which is calculated by fitting the profile obtained from the measurement sample (see Section 5.4).

The Hall voltage was computed for various base emitter voltages and is shown in Figs. 5.22 and 5.23. The abscissa, W' denotes the distance between an arbitrary point on the device surface and the corresponding point symmetric about $x = 0$. We note that as the level of injection increases, there is a shift in the Hall voltage peak away from the junction. The location of the peak is a function of the minority carrier concentration, $V_H \cong 1/n$. The concentration of the holes (although larger than that of the electrons) is reduced close to the junction vicinity and increases exponentially with increasing W'. At large W' however, the reduction in V_H is due to the shunting effects imposed by the presence of the base electrodes. At the vicinity of the junction, in particular the depletion zone, there is a reduction in the Hall coefficient, R_H and consequently the Hall voltage is smaller in magnitude ($p \geq n$). In the N+ emitter region, since n is large (and hence R_H very small) and furthermore being in close proximity to the emitter electrode, the Hall voltage is practically unobservable. These considerations are in line with the predictions of minimal Hall field near the N-P junction of the diode structure presented in [42]. Since the magnitudes of the carrier distributions are functions of the applied bias, the peak V_H varies with W' for the various injection levels. We also observe that the magnitude of the peak is directly proportional to the total device current. For the operating points shown, the maximum Hall voltage per unit of input current remains approximately constant (as in Hall plates). Figures 5.22 and 5.23, clearly illustrate the intricate combination of bipolar action and magnetic field, viz., the action of the Lorentz force on the injected minority and majority carriers. The results presented on the Hall voltage correspond to a direction of the Hall field that pertains to that of the majority carriers. For the device simulated, $p >> n$ in most parts of the base region.

Computations made for various operating voltages and magnetic field strengths show

that the Hall voltage is a linear function of magnetic field. In Fig. 5.23, we see the distribution of Hall voltage for $B = \pm 500$ mT and $V_{BE} = 0.85$ V. To illustrate the effects of magnetic field near the junction vicinity, equipotential lines for the region around the emitter of the device are shown in Fig. 5.24. The dashed lines indicate the interface between the semiconductor and the oxide at the surface and the bold line denotes the emitter electrode. The device is operated at $V_{BE} = 0.85$ V with a magnetic field of $B = 2$ Tesla parallel to the chip surface. The current through the device is 0.6 mA. The equipotential lines appear to be symmetric around the emitter base junction indicating that there are no Hall fields in that vicinity. The displayed area is approximately 29 μm in the x-direction and is symmetric about $x = 0$, and 5.5 μm from the oxide edge at the surface. The distribution of flow lines for minority carriers (electrons) is illustrated in Fig. 5.25 for operating conditions identical to those in Fig. 5.24. Unlike the distribution of potential, the effect of the magnetic field clearly manifests itself in the distribution of current density. The arrow indicates the direction of charge flow. The displayed area is approximately 21.5 μm × 4.5 μm of the device centre. There is no indication of asymmetry in the injected emitter current at the metallurgical emitter base junction.

5.5.2 Discussion of Measurement Results

The Hall voltage in the base region of the various MT samples were monitored as a function of the base emitter voltage for a 500 mT magnetic field. The results are illustrated in Fig. 5.26. The Hall voltages shown have been nulled by the corresponding zero field offset voltages.

At low injection levels $V_{BE} \cong 0.7$ V, the Hall voltages although small in magnitude, are larger in areas of base region that are closer to the junction (say at the vicinity of $W' \cong 40$ μm). As the level of injection increases, the Hall voltage peak shifts away from the junction, and is located at the vicinity of $W' \cong 60$ μm. At high injection levels $V_{BE} \cong 0.85$ V, the Hall voltages as

we see from Fig. 5.26 appear to be largest at $W' \geq 80$ µm. We note from the values of Hall voltage, that the direction of the Hall field in the base region (Fig. 5.26) is opposite to that obtained when the device was operated in the common-base configuration (Figs. 5.18 and 5.19)

5.5.3 Comparison of Numerical and Measurement Results

The current voltage characteristics resulting from the measurements and simulations are illustrated in Fig. 5.27. Apart from the general considerations given in [18], there can be many specific causes that contribute to the discrepancy between the measured and simulated current-voltage characteristics shown in Fig. 5.27. The most likely reasons are the following:

(i) the simplification of the device geometry that was made for purposes of an economic simulation. At the device's bottom and side edges, a no-flow condition on the current densities has been imposed. This is not consistent with the realistic structure because of the presence of a nonequilibrium P-N junction surrounding the base region (see Figs. 5.21 and 5.14). Furthermore, there may be possible leakage currents particularly at the upper sidewalls of the emitter base junction (in the vicinity of the junction/oxide interface) which can contribute significantly to the discrepancy at low injection levels. In addition, we are dealing with a two-dimensional numerical simulation, and consequently, the line current densities (A/cm) are assumed uniform in the z-direction. In the fabricated device, however, the emitter and base electrodes are of unequal length. Integrating the line current densities over the electrode lengths leads to a mismatch in the conservation of total device current. To maintain the conservation of currents in the numerical procedure, we have assumed that the electrode lengths, $L_B = L_E = 40$ µm. Also, there could be possible contact potentials at the electrodes which have been neglected in the simulations.

(ii) The models employed for the carrier mobilities and generation-recombination terms in the equations, might not be providing a true description of the physical processes taking

place in the fabricated device. In particular, effects due to high doping have not been accounted for.

(iii) Discrepancies in the distribution of impurity concentration. Knowledge of the true distribution of impurities can only be acquired if a two-dimensional measurement is performed. In particular, the distribution of acceptor concentration in the base region plays a crucial role in the Gummel number as well as the emitter injection efficiency. These parameters have a direct influence on the total device current.

In general, the various assumptions made in the equations and physical models could lead to errors that may cancel or add yielding discrepancies that may be large or small.

Comparison of the measured Hall voltages with the numerically simulated (ideal) Hall voltages are shown in Figs. 5.28 to 5.30 for V_{BE} = 0.7 V, 0.75 V, and 0.8 V respectively. The numerical results seem to adequately predict the general distribution of the measured Hall voltage for the various levels of injection. The Hall voltage distribution as a function of the base emitter voltage is discussed in Sections 5.5.1 and 5.5.2.

The discrepancies between the experimental and simulated results can again be attributed to a variety of reasons. An obvious cause of discrepancy stems from the fact that the measured and simulated device currents differ considerably (see Fig. 5.27). Since the Hall voltage in the device is proportional to the total device current (as discussed in Section 5.5.1), it is an exponential function of the applied voltage [$V_H \sim \exp(V_{BE})$]. Consequently, the errors in V_H become progressively larger with increasing applied voltage. Furthermore, in the fabricated device, the Hall probes are of a finite length as opposed to the infinitesimally small (i.e., ideal) probes that are used in the simulation. Also, offsets (voltage across probes at zero magnetic field) could result from geometrical imperfections in the probe electrodes (errors in mask alignment) or fabrication errors (overetching or under etching of contacts). Offsets could also result from the thermal and mechanical stresses arising from the packaging material of the die. The resulting piezoresistance effects could possibly produce potential gradients that cancel the Hall field. Offsets in the device are unfortunately a function of the

operating point as well as the magnetic field.

Nevertheless, immaterial of the discrepancies involved, the magnitudes of the Hall voltage obtained through either measurement or simulation are too minute to cause any asymmetric emitter injection.

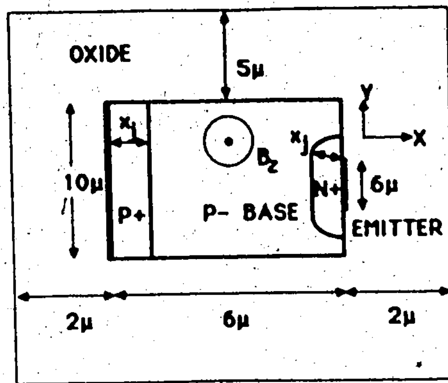

Fig. 5.1 Two-dimensional geometry of device enclosed by an artificial oxide region.

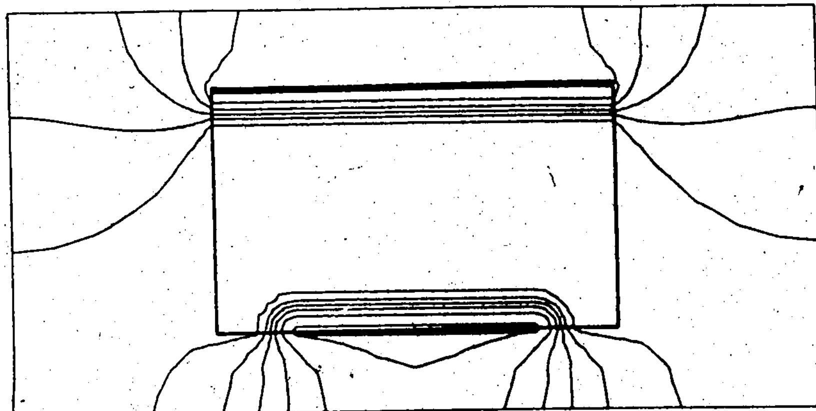
(a)

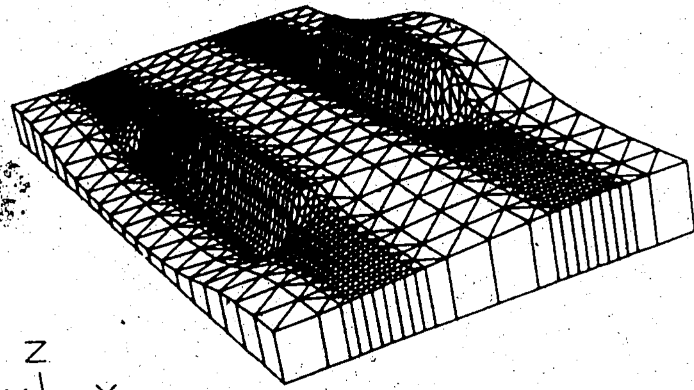

(b)

Fig. 5.2 (a) Equipotential lines and (b) potential distribution in the domain shown in Fig. 5.1.

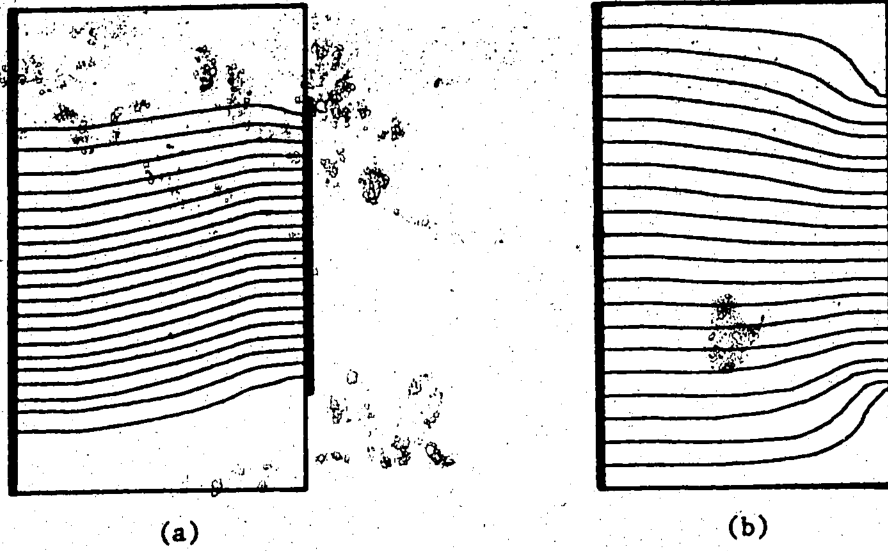

Fig. 5.3 Flow lines of current density for: (a) electrons injected from the emitter, (b) holes injected from base.

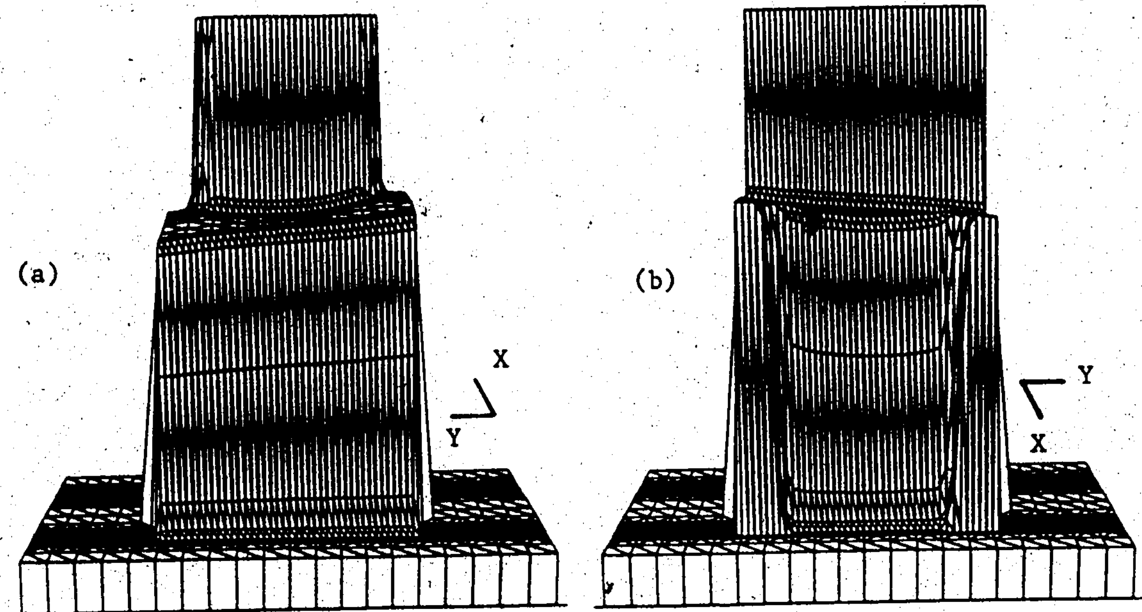

Fig. 5.4 The distribution of (a) electrons and (b) holes in the domain as shown in Fig. 5.2. The distributions have been clipped off at 10^{19} cm^{-3} at the respective N+ and P+ regions. In the oxide region, electron and hole concentrations are zero. Note that the direction of axes are opposite in both cases.

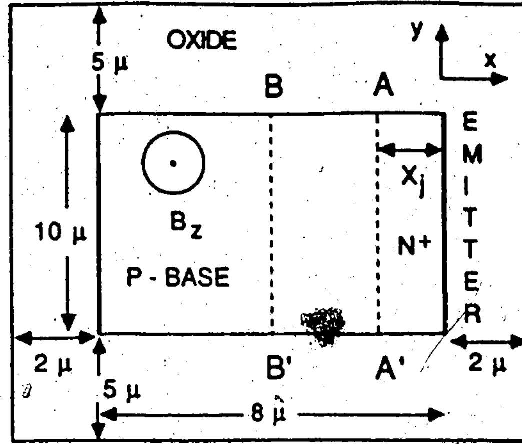

Fig. 5.5 Two-dimensional geometry of diode. AA' and BB' denote cut lines at $x = 6.75$ μm and $x = 5$ μm respectively.

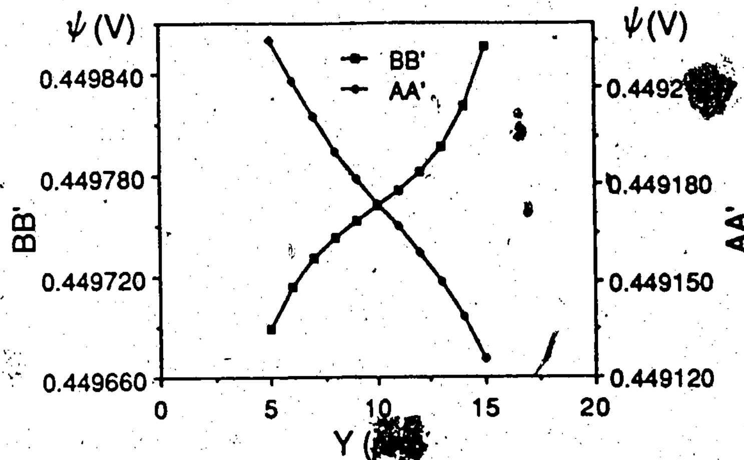

Fig. 5.6 Electrostatic potential distribution in diode (5 μm ≤ y ≤ 15 μm) at BB' and AA'. Device is operated at high injection, $V_{BE} = 0.9$ V, and $B = 2$ T.

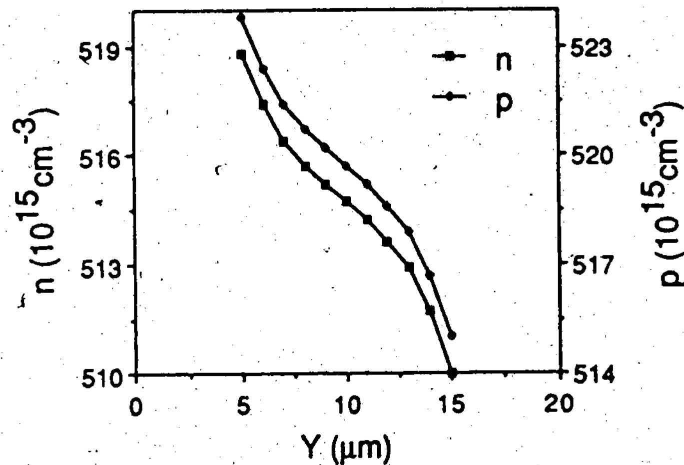

Fig. 5.7 Electron and hole concentrations in device at BB' operated at high

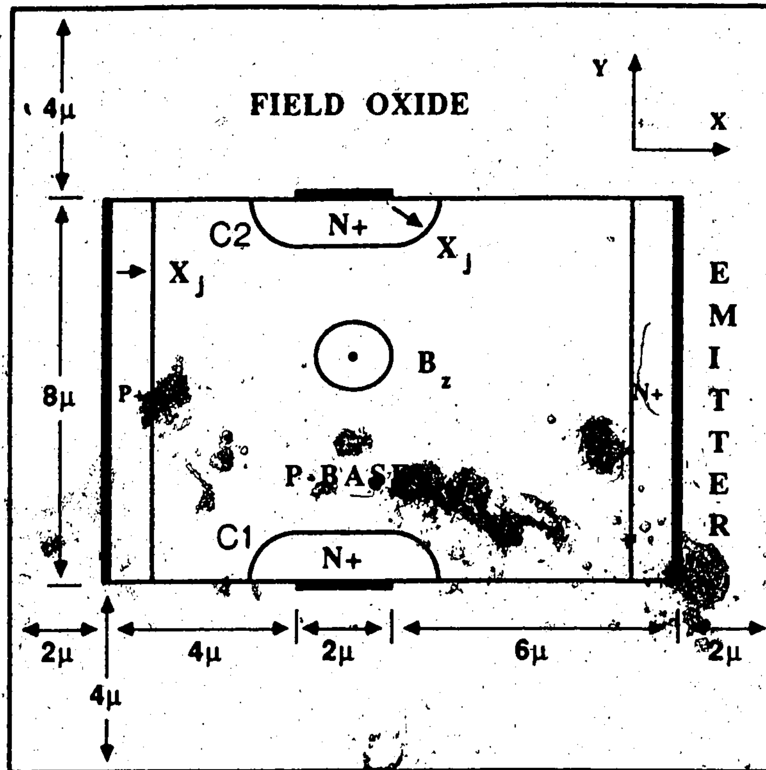

Fig. 5.8 Simulation geometry of dual-collector NPN magnetotransistor.

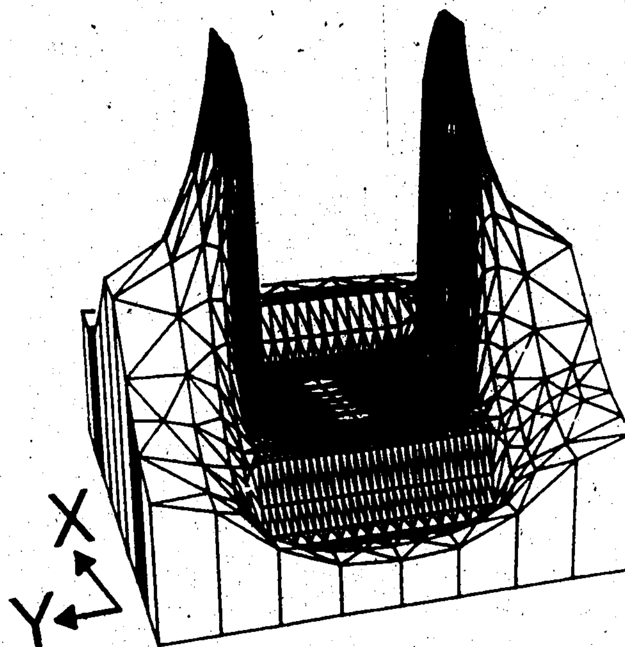

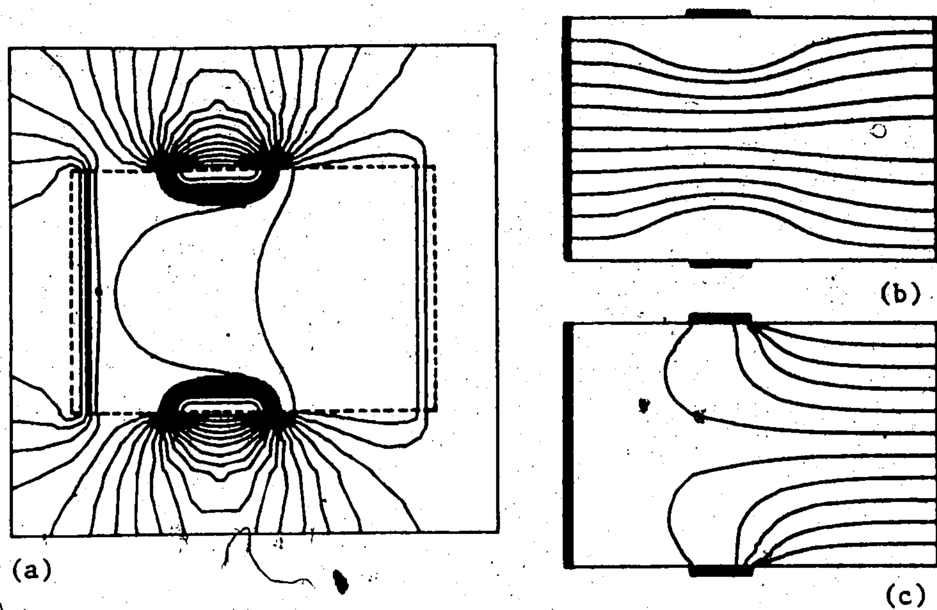

Fig. 5.10 (a) Equipotential lines. Current density flow lines of (b) holes injected from base (c) electrons injected from emitter. $V_{BE} = V_{CE} = 0.9$ V, and $B = 0$ T.

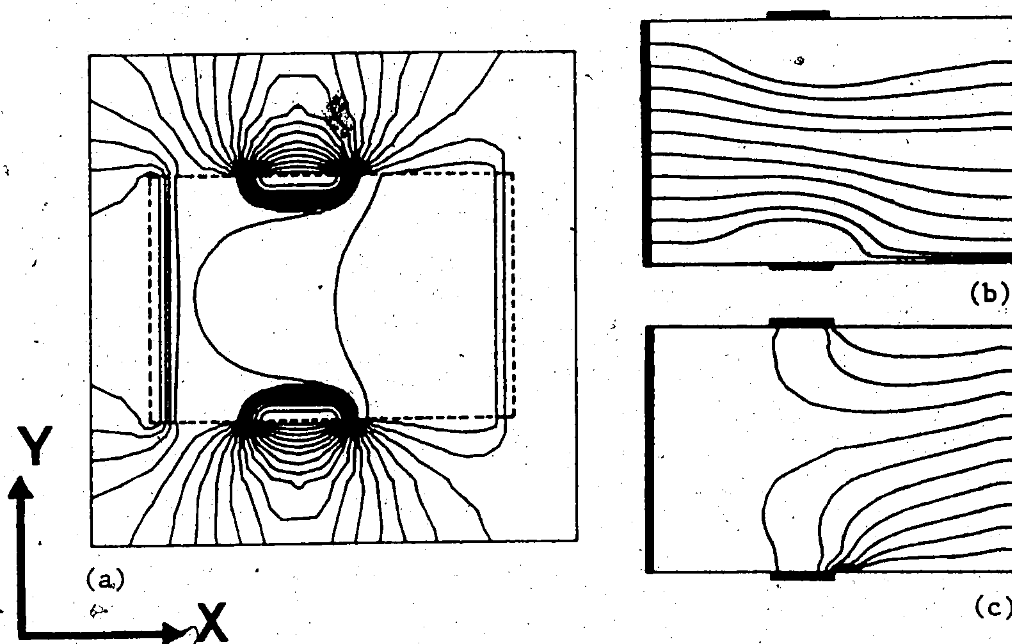

Fig. 5.11 As in Fig. 5.10, but for $B = 2$ Tesla.

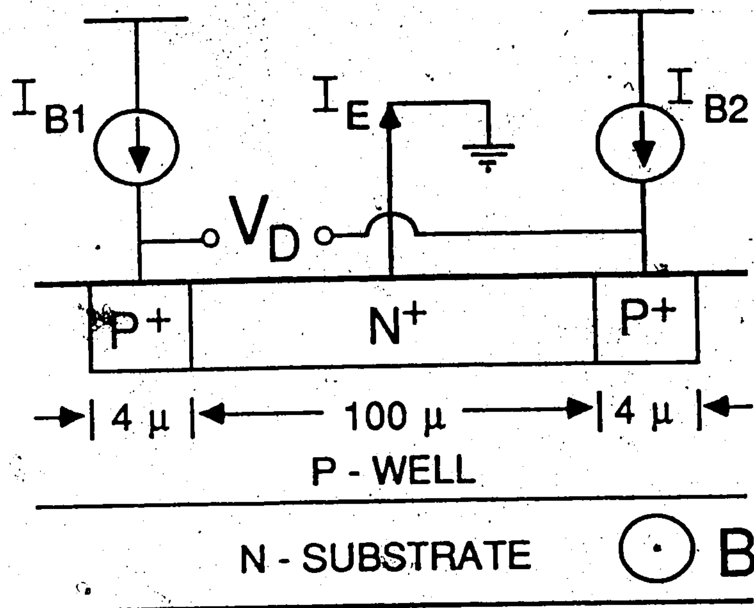

Fig. 5.12 Measurement schematic of differential voltage, V_D across the emitter base junction of the SSIMT. The magnetic induction, B is perpendicular to the direction of the injected current.

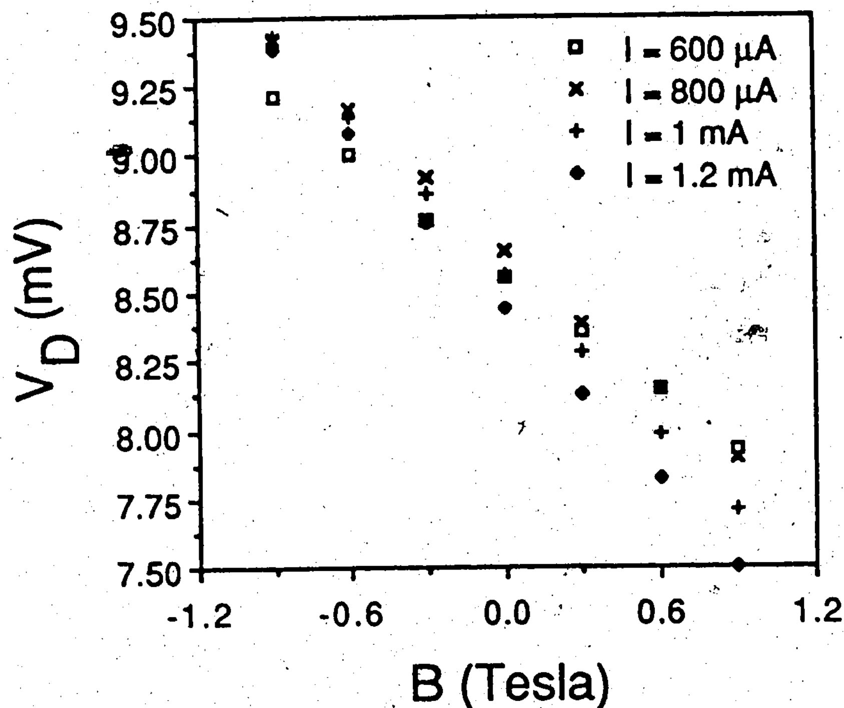

Fig. 5.13 The differential voltage as a function of magnetic induction

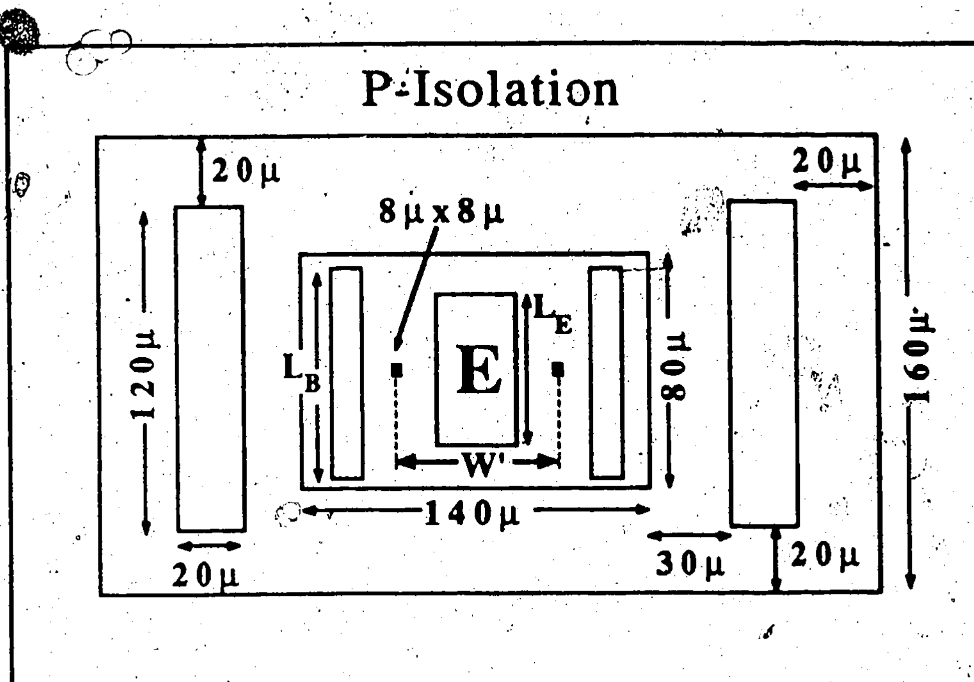

(a)

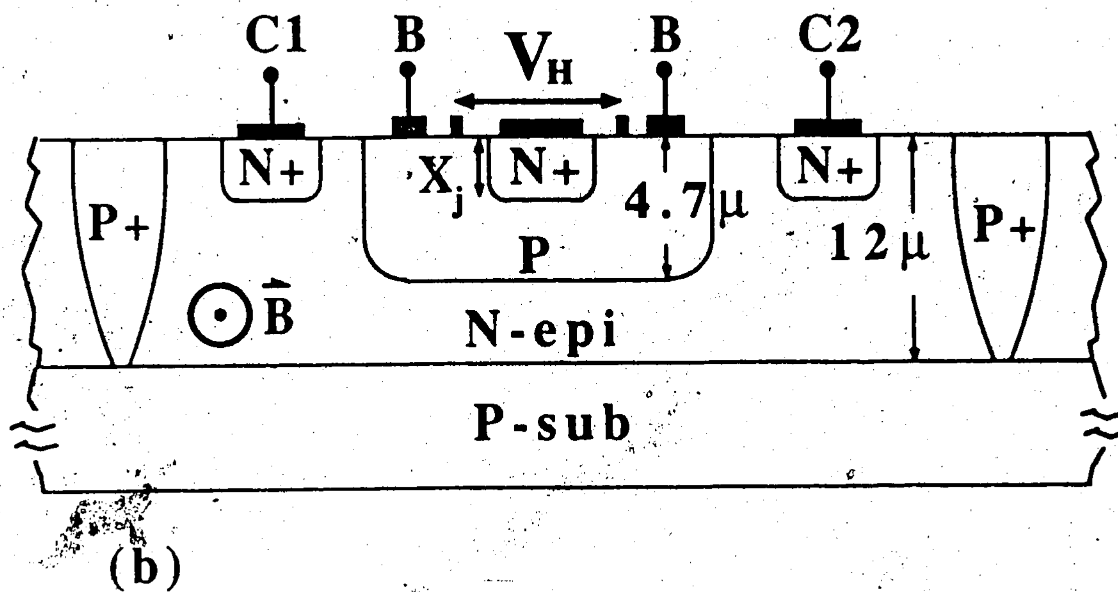

(b)

Fig. 5.14 (a) Top view and (b) cross-sectional view of the basic bipolar dual-collector MT geometry used in the measurements.

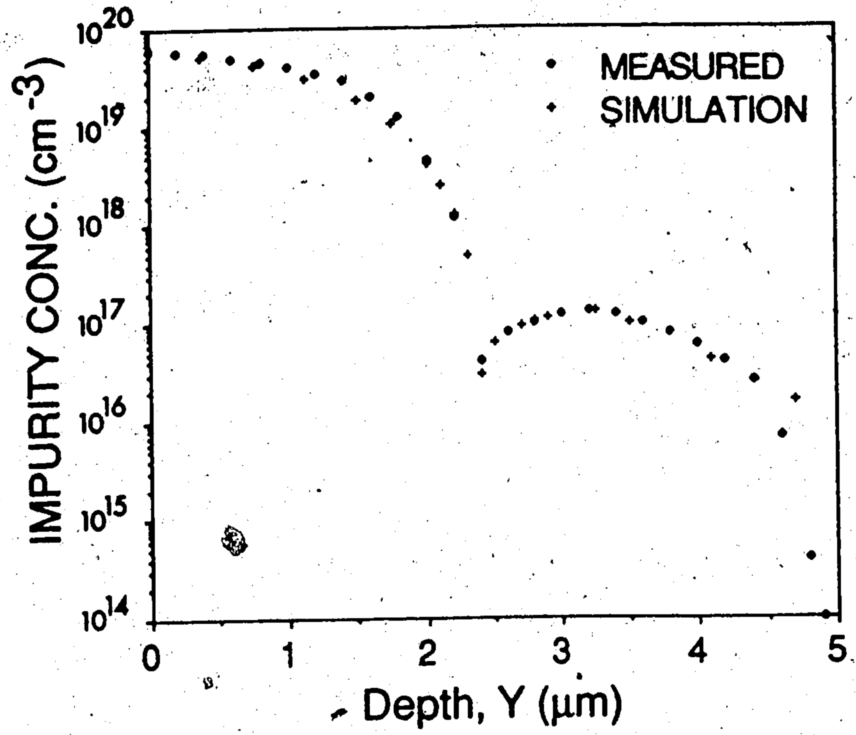

Fig. 5.15 The measured impurity profile at $x = 0$ for the device shown in Fig. 5.14. The profile used in simulations is discussed in Section 5.5.1.

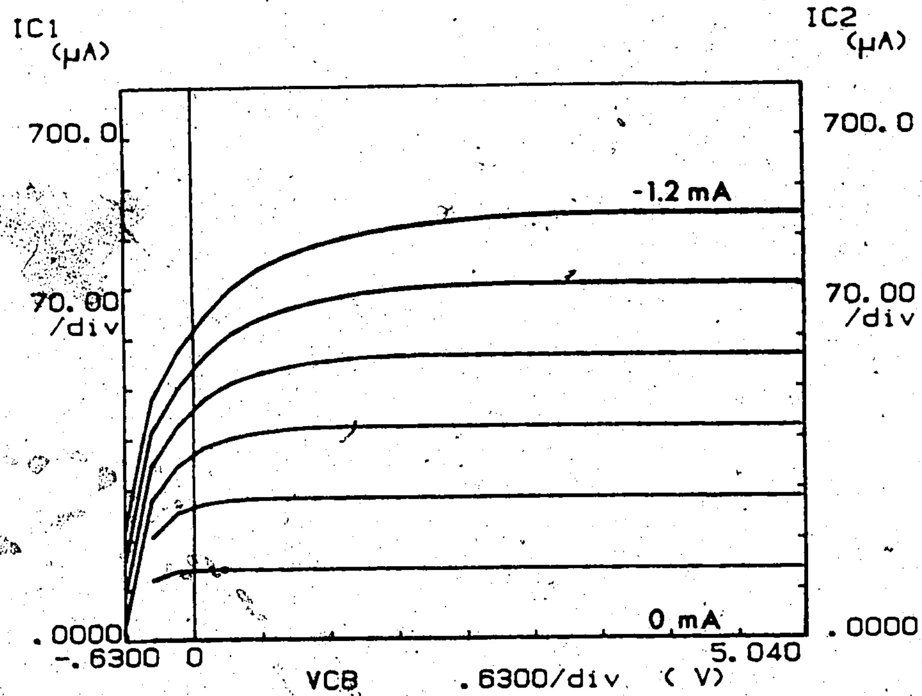

Fig. 5.16 Current-voltage characteristics for the MT in common-base

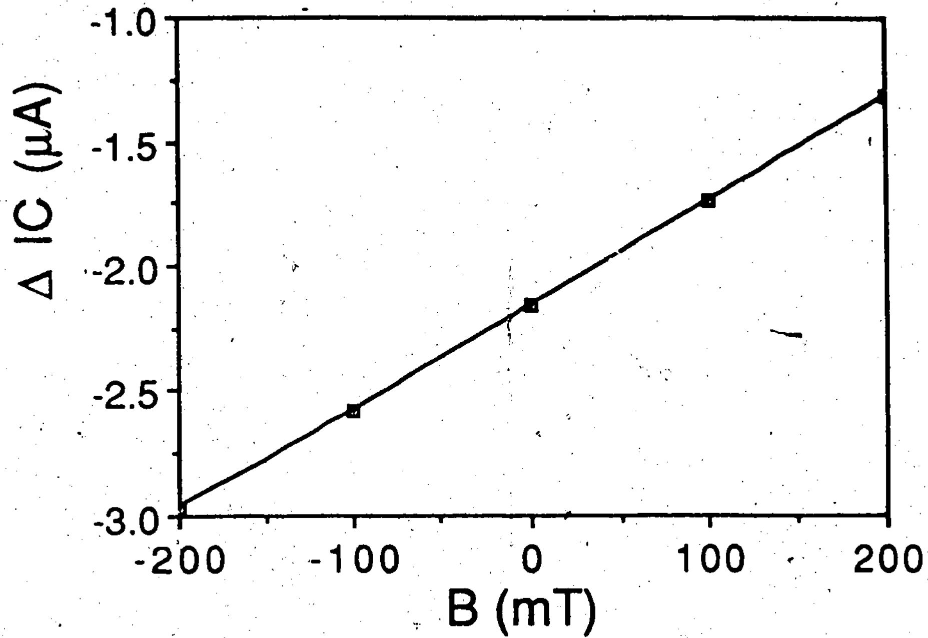

Fig. 5.17 Collector current imbalance, $\Delta I_C = (I_{C1} - I_{C2})$ as a function of field strength. The device is operated at $V_{CB} = 5$ V and $I_E = -1$ mA.

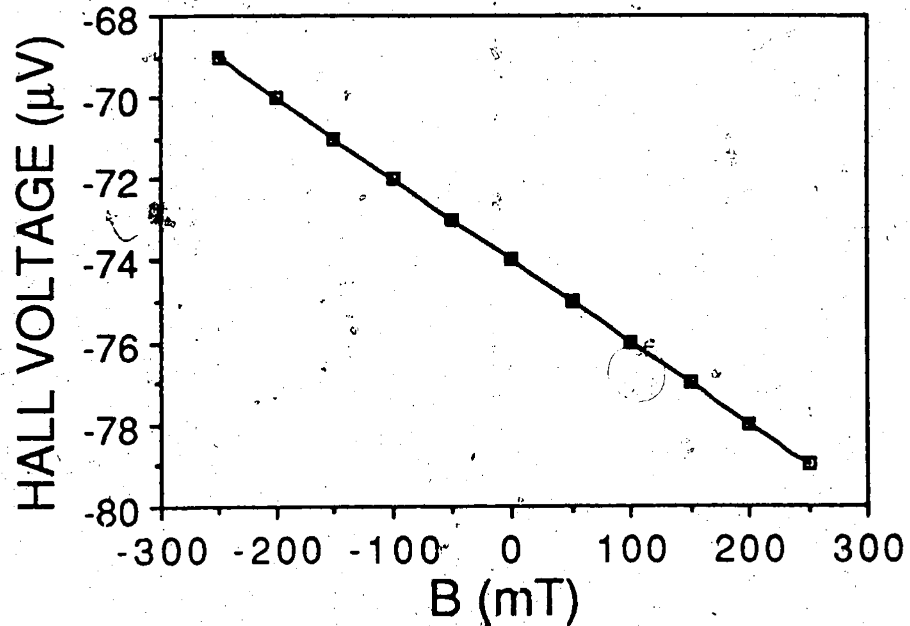

Fig. 5.18 The Hall voltage measured as a function of magnetic induction ($|B| \leq 250$ mT) for the MT with $W' = 40$ μm. The operating conditions of device are as in Fig. 5.17.

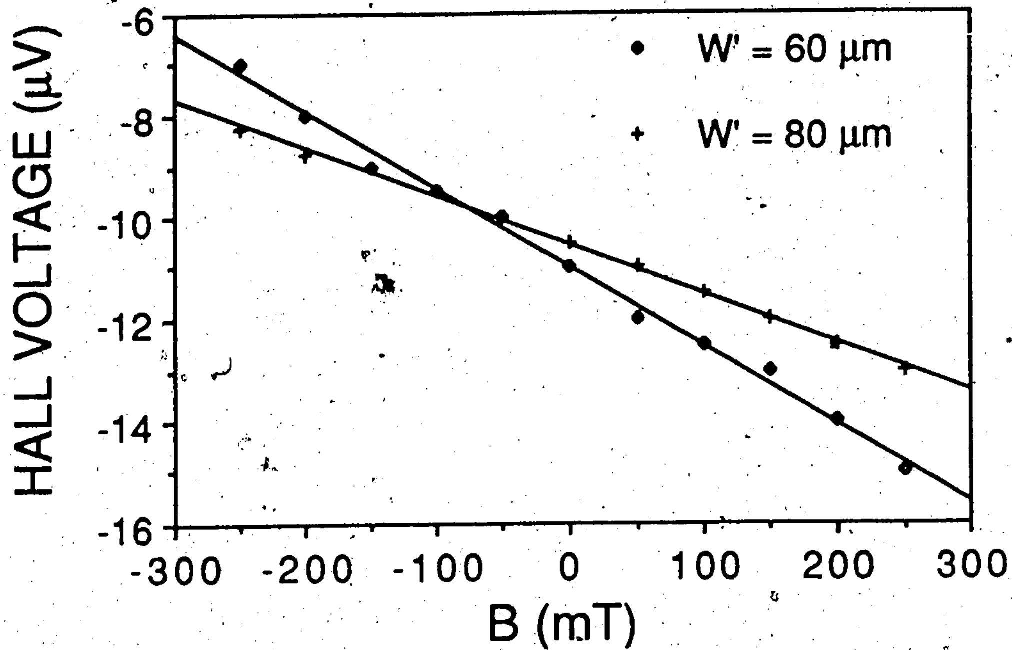

Fig. 5.19 As in Fig. 5.18 but for the MT's with $W' = 60$ μm and 80 μm.

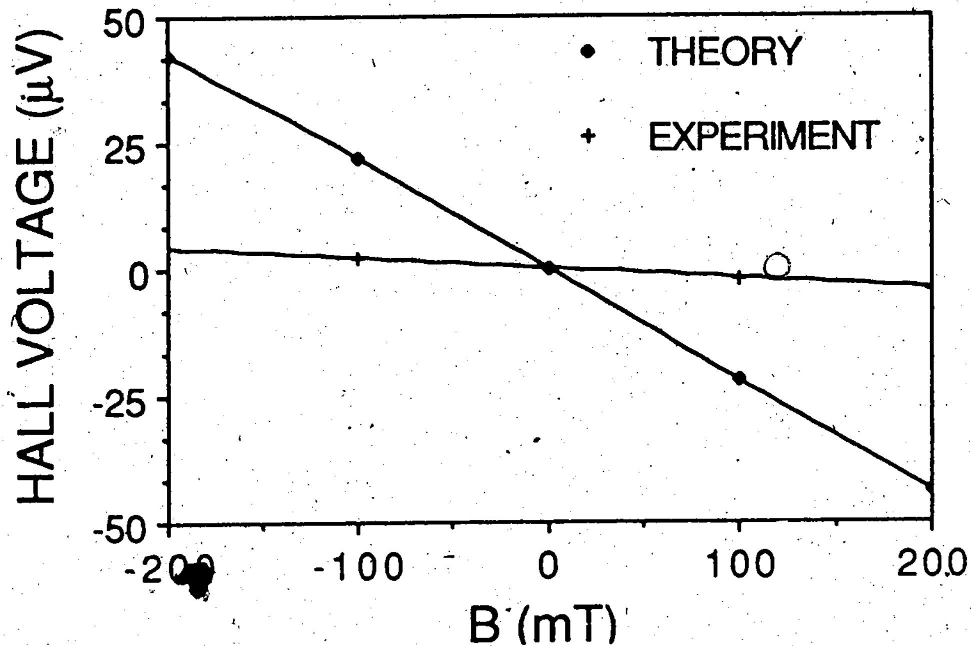

Fig. 5.20 Comparison of Hall voltages as a function of magnetic induction, obtained from the analytical model and measured using the MT with $W' = 40$ μm. The MT is operated at $V_{CB} = 5$ V and $I_E = -1$ mA.

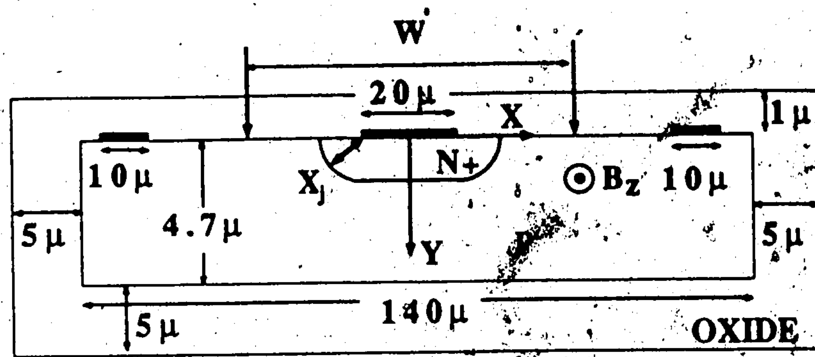

Fig. 5.21 Two-dimensional simulation geometry of the MT's base region surrounded by an artificial oxide region.

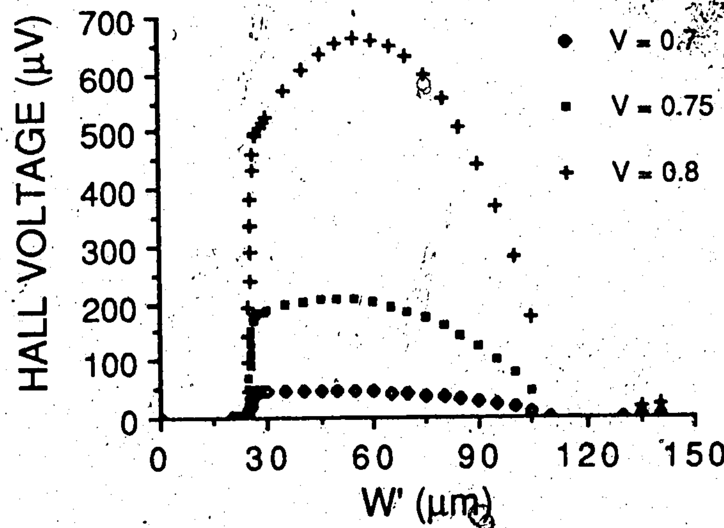

Fig. 5.22 The Hall voltage distribution as a function of position, W' (see Fig. 5.21) along $y = 0$, for various base emitter voltages and $B = 500$ mT.

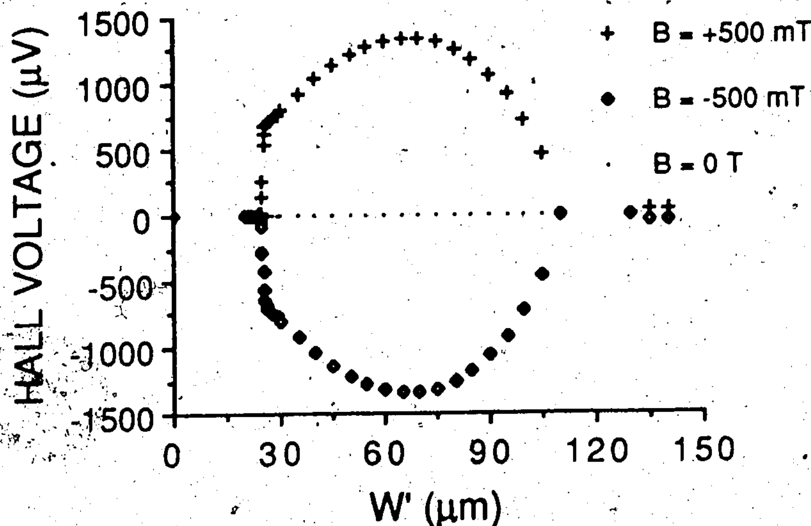

Fig. 5.23 The Hall voltage as a function of position at various field strengths for $V_{BE} = 0.85$ V.

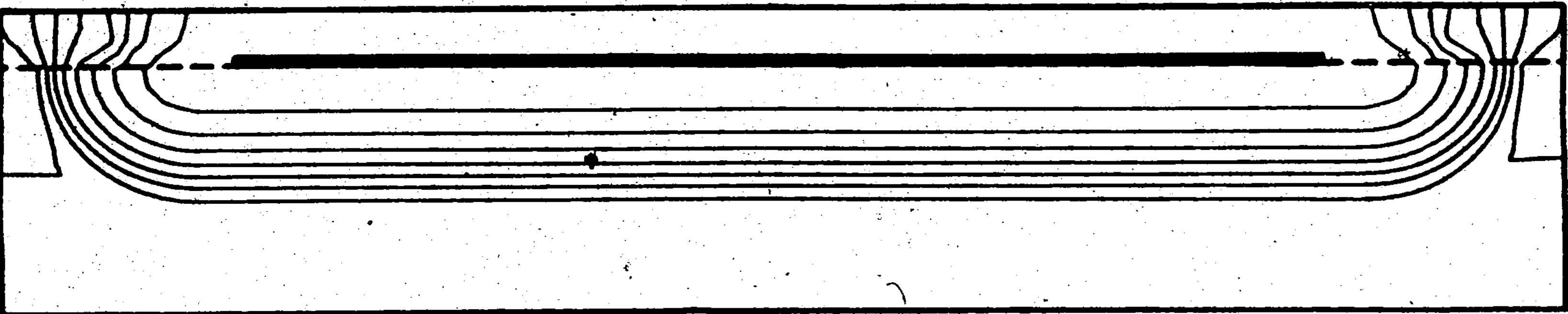

Fig. 5.24 Equipotential lines in the vicinity of the emitter for $V_{BE} = 0.85$ V and $B = 2$ T. The displayed area corresponds to $|x| \leq 14.5$ µm and -1 µm $\leq |y| \leq 4.5$ µm; see Fig. 5.21 for x and y orientations.

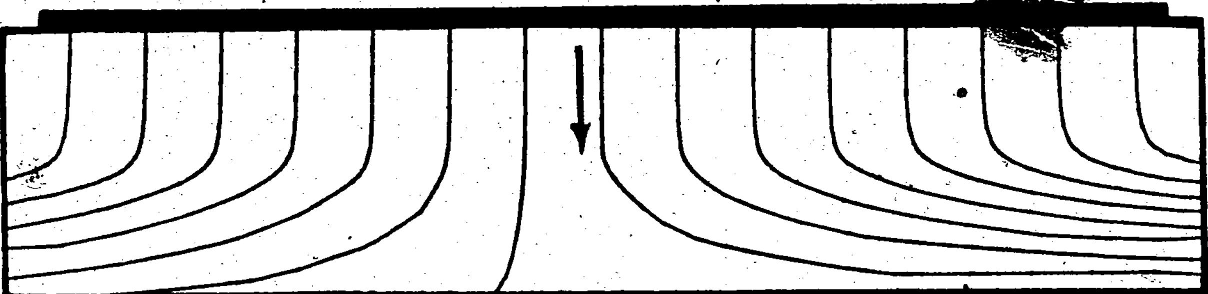

Fig. 5.25 Minority carrier (electron) flow lines in the vicinity of the emitter for $V_{BE} = 0.85$ V and $B = 2$ T. The displayed area corresponds to $|x| \leq 11$ µm and $0 \leq |y| \leq 4.5$ µm; see Fig. 5.21 for x and y orientations.

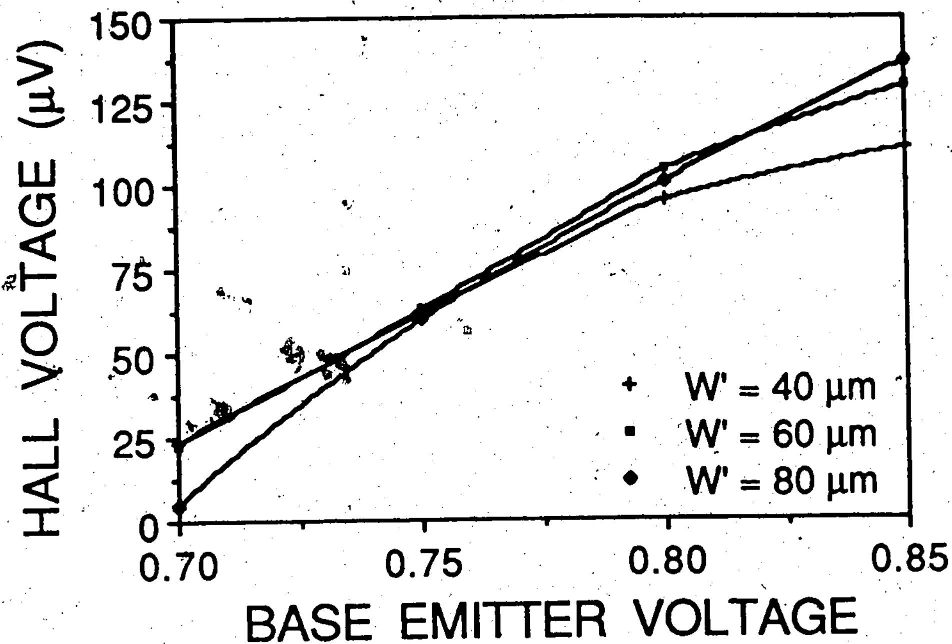

Fig. 5.26 The Hall voltage monitored as a function of injection level at $B = 500$ mT for the various MT geometries.

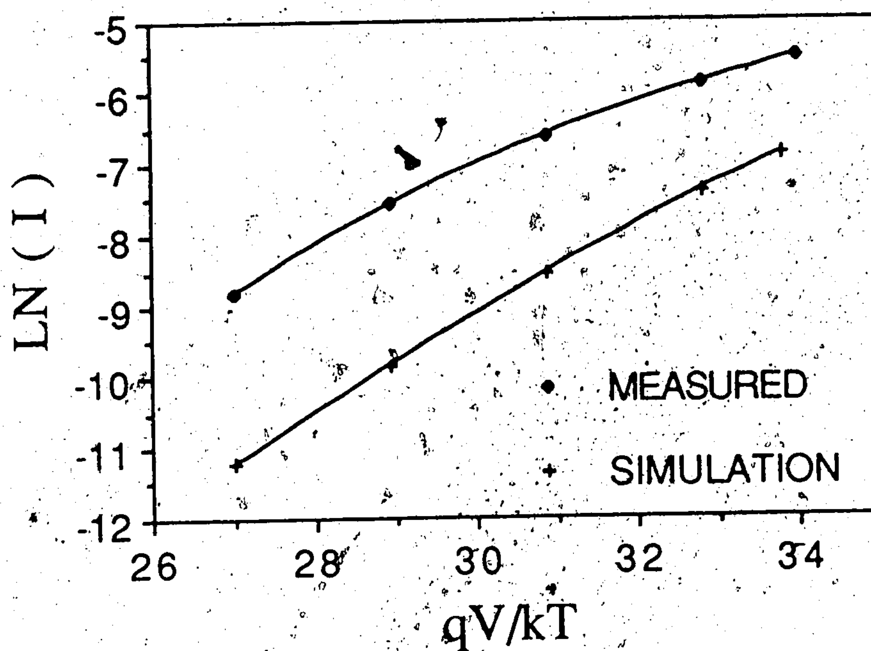

Fig. 5.27 Comparison of measured and simulated current-voltage characteristics for MT in common-emitter diode configuration.

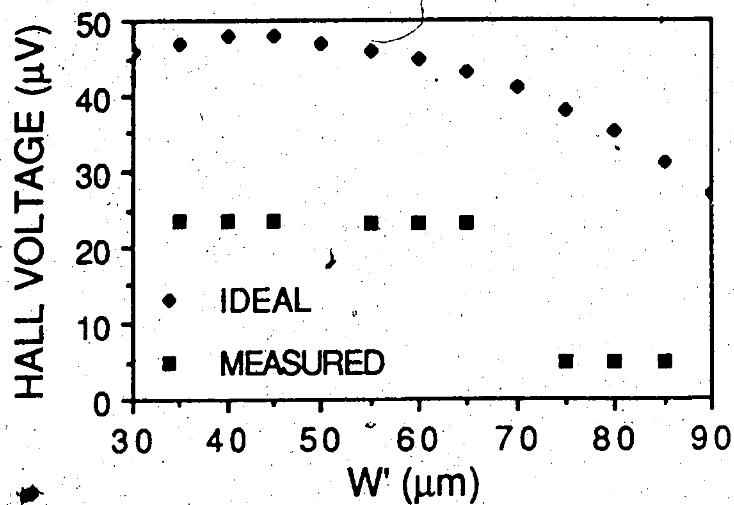

Fig. 5.28 Comparison of measured and simulated (ideal) Hall voltages for $V_{BE} = 0.7$ V and $B = 500$ mT.

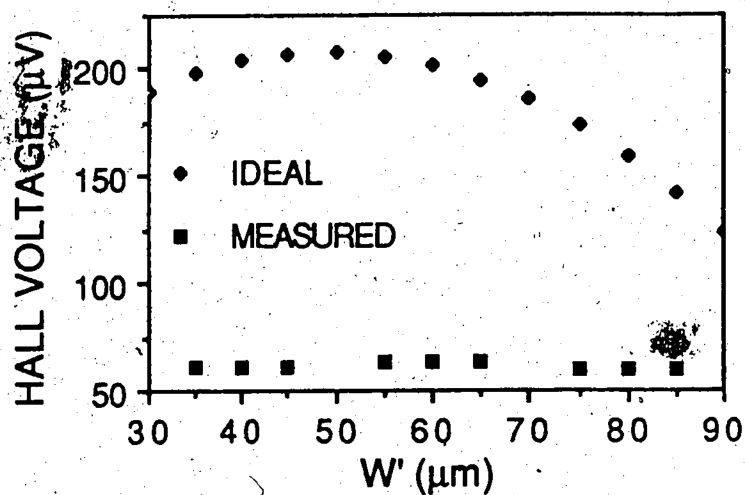

Fig. 5.29 As in Fig. 5.28 but for $V_{BE} = 0.75$ V.

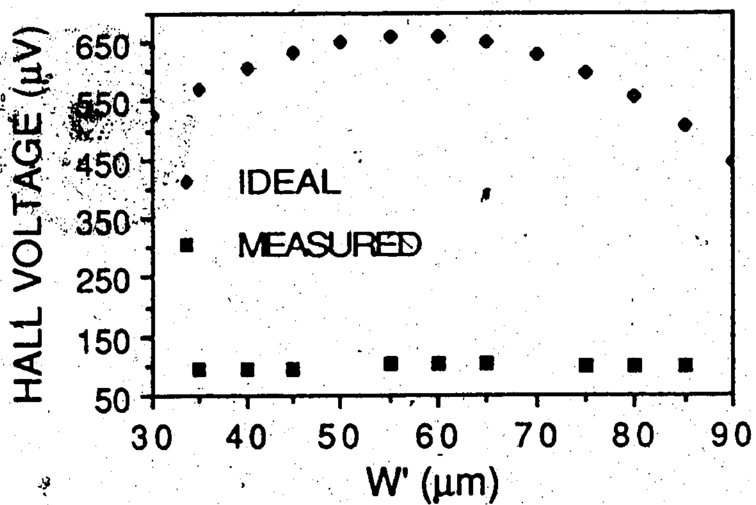

Fig. 5.30 As in Fig. 5.28 but for $V_{BE} = 0.8$ V.

6. 1/f NOISE IN MAGNETOTRANSISTORS

Most high sensitivity magnetotransistors reported hitherto [5] require large power. This makes the circuit designer's job particularly difficult because of the need to provide circuitry to compensate for the effects (extrinsic noise) caused by Joule heating. Besides the temperature induced effects, the offset in the output signal (introduced by geometric errors in fabrication, thermal and mechanical stresses) is one major component of extrinsic noise and in particular, can be temperature dependent. It is therefore desirable to operate the device at low current although this may compromise the magnetic sensitivity, i.e., the signal power. But there may be no significant deterioration of signal-to-noise ratio since the level of noise intrinsic to the device (such as 1/f or white noise) is correspondingly reduced at low device currents [6]. While extrinsic noise can be reduced by careful selection of design, fabrication, and operating conditions, intrinsic noise is a fundamental physical effect (indeterministic in nature) that ultimately limits the field resolution, B_{min}. In particular, at low frequency operation, 1/f noise can impose major restrictions on the application range of MT's.

6.1 Previous Noise Studies in Magnetotransistors

Noise in unipolar devices (e.g. the Hall plate) has received much more attention (see [43] and references therein) than noise in bipolar magnetic sensors. Results have been presented for thin film Hall plates [43], heterostructure Hall elements [44], and magnetic field sensitive field effect transistors (MAGFET's) [41].

In bipolar magnetic devices, noise studies have only been carried out for the magnetodiode [45] and the magnetotransistor [46,47]. Power spectral density measurements of voltage fluctuations in silicon-on-sapphire (SOS) and germanium magnetodiodes were presented in [45] for various device geometries and operating conditions. Calculations based on measurements yielded B_{min} in the order of 0.1 μT/√Hz at 1 kHz, for a sensitivity of 10 V/T at 1 mA of device current. Since magnetodiodes rely on the magnetoconcentration effect (magnetic field modulation of base conductance), the 1/f noise was found to be a function of

the magnitude and direction of the magnetic field. The source of $1/f$ noise in such devices was consequently attributed to fluctuations in the base conductance. For dual-collector magnetotransistors [46], the measured differential signal-to-noise ratio (SNR) was in the order of 2×10^4 /T for a bandwidth of 1 MHz, yielding B_{min} of 50 μT/√Hz. However, there were no reports on the behaviour of the individual collector noise voltages or on their statistical interdependence. Calculations as well as measurement results of SNR for various single collector lateral MT structures were presented in [47]. The calculations considered just the shot noise in the collector and measurements yielded B_{min} of 0.4 μT/√Hz at 10 Hz for a sensitivity of 1.5 /T and 600 μA of current.

6.2 Device Description

A variety of dual-collector bipolar and CMOS MT structures, sensitive to magnetic fields parallel to the chip surface were used for the noise measurements. The CMOS MT was fabricated using the Northern Telecom's standard 5 μm process (see Fig. 6.1). The junction depths for the N+ and P+ diffusions are 1 μm and 0.9 μm respectively, and that for the P-well it is approximately 10 μm. The impurity concentration is approximately 10^{16} cm^{-3} in the P-well and 2×10^{15} cm^{-3} in the N-substrate. The device has predominantly vertical emitter injection since lateral injection is significantly suppressed by the placement of a pair of planar P+ stripes along emitter sidewalls as in the SSIMT structure presented in [1]. In the presence of a magnetic field parallel to the chip surface, the minority carriers injected from the bottom wall of the emitter experience a deflection because of the Lorentz force and consequently give rise to an imbalance in collector current. The collectors, C1 and C2 serve as output terminals for the signal. Since the collectors are in the N-substrate, the device is somewhat shielded from any neighbouring active components by a P-ring (R) with reverse bias ring-substrate voltage. When operated in common emitter configuration, the device yields a maximum sensitivity, S of 5.6 %/T for device currents less than 1 mA. The sensitivity, S of the device to the field is

defined by expression (2.1). The relative nonlinearity in ΔI_C ($= I_{C1} - I_{C2}$) is less than 1 % for fields up to 1 Tesla.

The counterpart of the CMOS magnetotransistor is fabricated in bipolar technology (see Fig. 5.14). Due to the nature of the doping distribution in the P-base region of the bipolar structure, the device operation is somewhat similar to that of the CMOS MT. The details of device operation and fabrication conditions are discussed in Section 5.4. It is assumed that the effect of the pair of 8 μm × 8 μm Hall probes (which were left unactivated in the course of our noise measurements), on the collector noise voltage power spectral densities (PSD) is negligible. The MT's of the two technologies (Figs. 6.1 and 5.14) differ in magnetic characteristics (such as output sensitivity to B), but the zero magnetic field electrical characteristics are almost identical.

6.3 Measurement Procedure

Denoting the discretely sampled noise voltage at time t by $v_n(t)$ and its Fourier transform (angular frequency, $\omega = 2\pi f$) by the complex function, $V_n(\omega)$, viz.,

$$V_n(\omega) = \int dt\, e^{-j\omega t}\, v_n(t). \tag{6.1}$$

The single-ended noise voltages of collectors C1 and C2 and their respective Fourier transforms are denoted by $v_{n1}(t)$, $v_{n2}(t)$ and $V_{n1}(\omega)$, $V_{n2}(\omega)$ respectively. Using a spectrum analyser, the single-ended PSD's $S_{11}(\omega)$ and $S_{22}(\omega)$ are measured, e.g.

$$S_{11}(\omega) = < V_{n1}(\omega)\, V^*_{n1}(\omega) >, \tag{6.2}$$

where < > denotes the ensemble average and the asterisk the complex conjugate. The differential PSD between the two collectors, viz.,

$$S_D(\omega) = < [V_{n1}(\omega) - V_{n2}(\omega)]\,[V_{n1}(\omega) - V_{n2}(\omega)]^* >, \tag{6.3}$$

is also measured. From (6.2) and (6.3), the real part, $Re\,[S_{12}(\omega)]$ of the cross spectral density

$$S_{12}(\omega) = < V_{n1}(\omega)\, V^*_{n2}(\omega) > \tag{6.4}$$

can be derived, because

$$S_D(\omega) = S_{11}(\omega) + S_{22}(\omega) - 2\,Re\,[S_{12}(\omega)]. \tag{6.5}$$

Since it is found that $S_{11}(\omega) = S_{22}(\omega)$, the

$$Re\,[S_{12}(\omega)] = S_{11}(\omega) - S_D(\omega)\,/\,2, \tag{6.6}$$

or the relative cross spectral density

$$Re\,[S_{12}(\omega)]\,/\,S_{11}(\omega) = 1 - S_D(\omega)\,/\,2\,S_{11}(\omega) \tag{6.7}$$

can be evaluated.

Recalling definition (6.1), the single-ended PSD is the Fourier transform of the respective time autocorrelation, e.g.

$$S_{11}(\omega) = \int d\tau\, e^{-j\omega\tau}\, C_{11}(\tau) \tag{6.8}$$

with

$$C_{11}(\tau) = < v_{n1}(t)\, v_{n1}(t+\tau) > \tag{6.9}$$

on the assumption that $v_n(t)$ is an ergodic process. Similarly, the cross-spectral density $S_{12}(\omega)$ and the mutual time correlation

$$C_{12}(\tau) = < v_{n1}(t)\, v_{n2}(t+\tau) > \tag{6.10}$$

form a Fourier transform pair. Unfortunately, measurement of $S_{11}(\omega) = S_{22}(\omega)$ and $S_D(\omega)$ allows only the real part of $S_{12}(\omega)$ to be obtained; thus $C_{12}(\tau)$ cannot be retrieved by Fourier inversion of $S_{12}(\omega)$. However, the correlation coefficient

$$\gamma = < v_{n1}\, v_{n2} > (< v^2_{n1} > < v^2_{n2} >)^{-1/2} \tag{6.11}$$

can be evaluated from the oscilloscope observation of $<v^2_{n1}>$, $<v^2_{n2}>$, and

$$< v^2_{nd} > = < (v_{n1} - v_{n2})^2 >, \tag{6.12}$$

and by using the relation

$$\gamma = 1 - < v^2_{nd} > / 2 < v^2_{n1} > \tag{6.13}$$

which was obtained by virtue of the observed property, $<v^2_{n1}> = <v^2_{n2}>$.

The PSD measurements are performed with the batteries, device under test (DUT), and the low noise amplifier (LNA) shielded by 0.375 inch steel container as shown in Fig. 6.2 [41]. To reduce the coupling between the LNA and DUT, each have a separate power supply (sealed lead acid batteries). Low frequency current blocking is achieved with high pass RC filters (HPF) which have a corner frequency of 0.03 Hz. The load and filter resistors are of the low noise metal film type. Also, low noise metalized polyester film capacitors are used in the filters. The LNA is a Brookdeal 5006 differential amplifier, which can also be used in single input mode. It has a fixed gain of 60 dB $\pm$ 0.3 dB, while its bandwidth is 0.1 Hz to 1 MHz. Noise voltage PSD's for the LNA are shown in Fig. 6.3 for the single ended and differential measurement modes with 221 kΩ resistors placed between the amplifier inputs and ground. The amplifier output is connected to an HP 3561A dynamic signal analyser (DSA). The DSA employs a fast Fourier transform algorithm to calculate spectra from d.c. to 100 kHz. To ensure relatively narrow band measurements, the PSD's are constructed from measurements performed on smaller frequency spans [41]. In the PSD plots 0.0 dB corresponds to 1.0 V RMS.

To obtain an approximate rms value, $<v^2_n>^{1/2}$ of the noise voltage in the time domain, the LNA output can be connected to an oscilloscope. It is assumed that v_n follows a Gaussian probability distribution and the technique outlined in [48] is used for obtaining $<v^2_n>^{1/2}$ from oscilloscope inspection. In this way, $<v^2_{n1}>^{1/2} = <v^2_{n2}>^{1/2}$ and $<v^2_{nd}>^{1/2}$ are determined. These rms noise voltages are subsequently used to investigate the degree to which the output noise in the MT collectors are correlated by retrieving the coefficient γ using eqn. (6.13).

6.4 Correlation in Collector Noise Voltages

Measurements of noise spectra obtained for the single ended and differential collectors of MT's fabricated in both CMOS and bipolar technologies are illustrated in Figs. 6.4 and 6.5 respectively. Measurements performed for $|B| \leq 0.5$ Tesla, indicate that the noise in the MT is not explicitly a function of magnetic field (as in magnetodiodes [45]), but rather is directly related to the magnitude of the output current. It is noted that this is only true for MT's which rely on carrier deflection to provide the signal. Carrier deflection is characterised by an output response which is linear with the magnetic field.

From Figs. 6.4 and 6.5, the differential collector noise voltage is observed to be at least two orders of magnitude smaller than the single ended collector noise for most part of the frequency spectrum. The MT fabricated in CMOS technology is biased with $I_B = 20\ \mu A$, $I_{C1} = I_{C2} \approx 975\ \mu A$, $V_{CE} = 4$ V, and $R_L = 3.3\ k\Omega$. The PSD's for the two measurement modes are illustrated in Fig. 6.4. The MT fabricated in bipolar technology is biased with the same base current but with $I_{C1} = I_{C2} \approx 760\ \mu A$, $V_{CE} = 7.7$ V, and $R_L = 6.75\ k\Omega$. The single ended and differential collector noise voltage PSD's are shown in Fig. 6.5. The individual collectors of the respective MT's have identical spectra, $S_{11}(\omega) = S_{22}(\omega)$ and they all follow an approximate $1/f$ type spectrum. For frequencies less than 10 kHz, the differential collector noise voltage PSD, $S_D(\omega)$ is about 50 dB lower than its single ended counterpart in the CMOS device. In the case of the bipolar MT, the difference appears to be 40 dB.

From inspection of Figs. 6.4 and 6.5, we learn that for frequencies, 1 Hz $\leq f \leq$ 100 kHz, and for both fabrication technologies, the differential PSD is much smaller than the single ended PSD, viz.,

$$S_D(\omega) \leq 10^{-4}\, S_{11}(\omega). \tag{6.14}$$

Using eqn. (6.7), one can conclude a strong positive correlation between the collector noise voltages, viz.,

$$Re\,[S_{12}(\omega)]\,/\,S_{11}(\omega) \sim 1.0. \tag{6.15}$$

Similarly, it was found that $<v^2_{nd}> \leq 0.1 <v^2_{n1}>$ from oscilloscope measurements, and hence $0.95 \leq \gamma \leq 1.00$, by using eqn. (6.13).

These results are in striking contrast to the case of the dual-drain MAGFET, where the differential spectral densities are *larger* than the single ended ones and a *negative* correlation, $Re\,[S_{12}(\omega)]/S_{11}(\omega)$ of about – 0.9 is found [41].

Based on the measured results of noise voltage PSD's shown, the signal-to-noise ratio for the CMOS MT for both differential and single ended measurement modes was evaluated. With eqn. (2.1) and an external load R_L connected to the collectors, the differential collector voltage ΔV_C can be expressed as

$$\Delta V_C(B)\,/\,B = S\,I_C\,R_L \tag{6.16}$$

where $\Delta V_C(B)/B$ turns out to be 0.4 V/T for I_C = 1.95 mA and R_L = 3.3 kΩ. Hence, the differential signal-to-noise ratio (√Hz/T) reads

$$\text{SNR} = S\,I_C\,R_L\,/ < v^2_{nd} >^{1/2}. \tag{6.17}$$

The field resolution, B_{min} is then determined by taking SNR = 1. At 1 kHz, the rms differential collector noise voltage is approximately 10 nV/√Hz, which yields a SNR of 4×10^9 √Hz/T. The field resolution, B_{min} for unity bandwidth for the given SNR is in the order of 25 nT. In the case of the single ended collector, the signal, $(\Delta V_C/2)$ is 0.2 V/T, and the rms collector noise voltage is about 4 μV/√Hz which yields a signal-to-noise ratio that is four orders of magnitude lower than the differential operation. For unity bandwidth, B_{min} turns out to be 14 μT.

To illustrate the uniqueness of the noise property in such structures, the performance of the CMOS MT operated in the differential mode is compared to two previous MT's that have

been reported [46,47]. The CMOS MT has a sensitivity of 0.06 /T (inferior to that studied in [47] by a factor of 300) but the field resolution is superior by a factor of 2 at 10 Hz, viz., 0.25 μT/√Hz compared with 0.4 μT/√Hz [47]. The field resolution at higher frequencies (away from the $1/f$ regime) is even more superior. Over a bandwidth of 5 MHz, the signal-to-noise ratio is 4.5×10^4 /T yielding B_{min} of 22 μT compared with the SNR of 2×10^4 /T ($B_{min} = 50$ μT) for a device with a sensitivity of 30 V/T [46].

The differences in correlation of output voltage fluctuations in the dual-collector MT and the dual-drain MAGFET [41] may be intuitively interpreted as follows. In the case of the dual-collector MT, the device noise current is governed by events localised at the emitter base junction vicinity. This manifests itself as fluctuations in the emitter injected current, equally felt by both the collectors. For the dual-drain MAGFET, fluctuations in the drain current are due to noise sources distributed throughout the conducting channel, while effects of the noise mechanisms at the source end are minimal. The carriers at the vicinity of the channel pinch-off undergo the partition effect, i.e. they land on one drain or the other. Consequently, the fluctuation at one drain is complemented by a fluctuation in the opposite sense at the other drain.

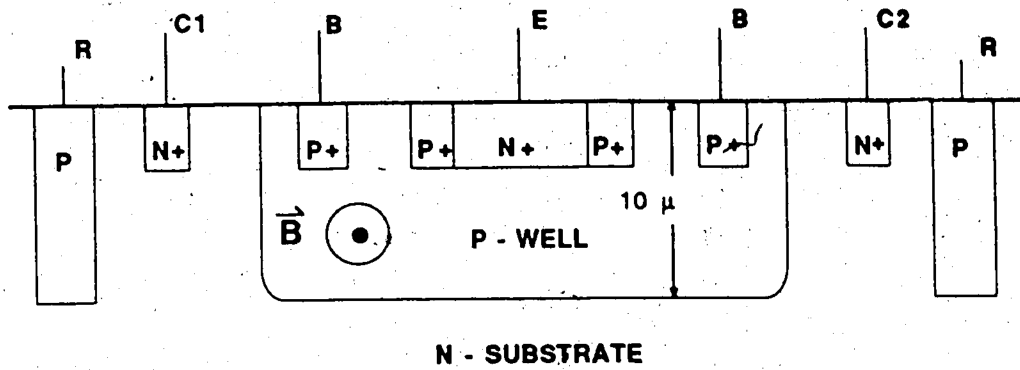

Fig. 6.1 Cross-sectional view of CMOS magnetotransistor sensitive to fields parallel to chip surface.

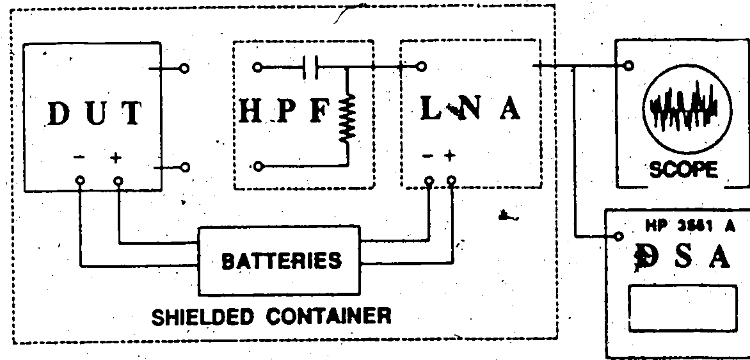

Fig. 6.2 Schematic of noise measurement system.

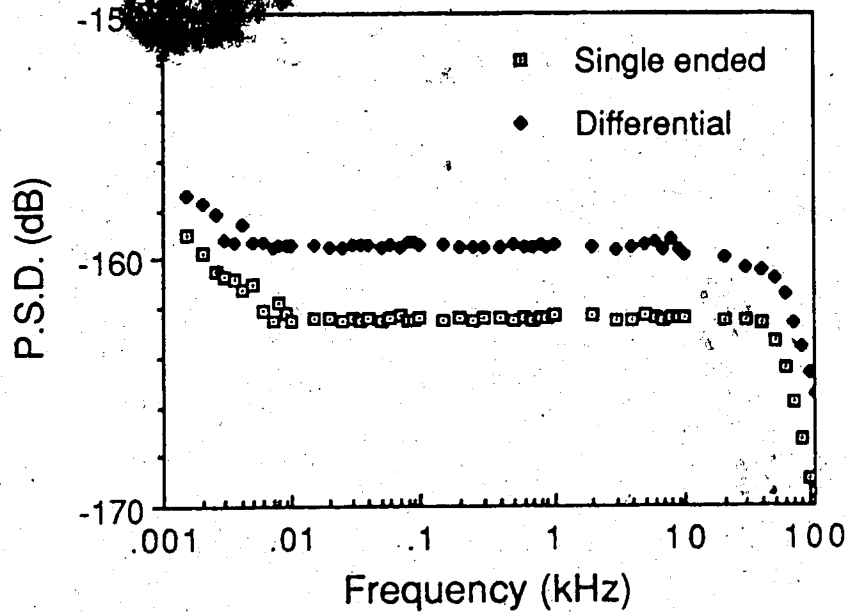

Fig. 6.3 Noise voltage power spectral density of low noise amplifier

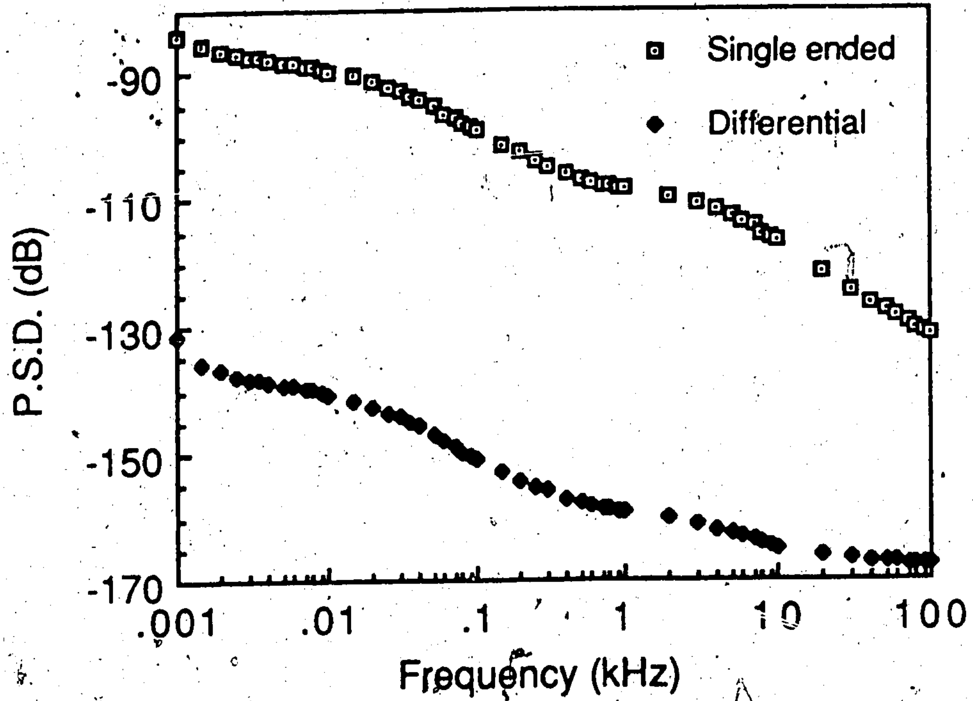

Fig. 6.4 The single ended and differential collector noise voltage PSD's for the MT fabricated in CMOS technology.

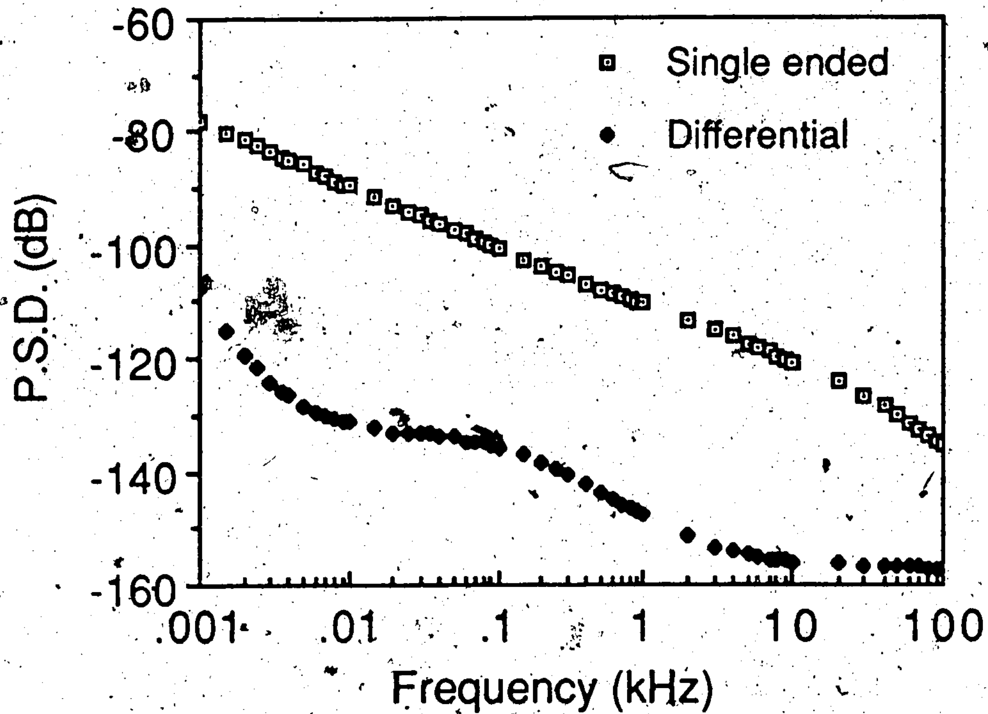

Fig. 6.5 As in Fig. 6.4 but for MT fabricated in bipolar technology.

CONCLUSIONS AND OUTLOOK

The analysis of carrier transport in magnetotransistors, up to this point in time, has been in terms of simple intuitive physical models. While some of these models can be verified in favourable cases by the solution of the full carrier transport equations, and thus remain as valuable heuristic tools, inconsistencies arise when an explanation of the magnetic sensitivity for general geometries and fabrication as well as operating conditions is attempted. The complex combination of galvanomagnetic and bipolar effects requires solutions of the transport equations in at least two-dimensions for accurate MT analysis.

In this regard, the work presented here describes the analysis of magnetotransistor operation using a two-dimensional numerical model. Results based on high precision computations (± 0.5 μV stopping criterion), show no trace of asymmetric minority carrier injection at the emitter. The Hall fields that were computed at the emitter base junction vicinity, are too weak in magnitude to substantiate the validity of the intuitively derived emitter injection modulation model. Measured data obtained using novel Hall probes procedures are in support of the predictions derived from the numerical analysis. If one likes to interpret the modeling results in terms of simple intuitive models, then carrier deflection should be chosen in the case of linear MT response, while magnetoconcentration seems to be adequate to describe possible nonlinearities.

Measurements of 1/*f* noise obtained for dual-collector MT's fabricated in CMOS and bipolar technologies, show a strong positive correlation (close to 100 %) between the noise voltages of the collectors. This unique correlation in the noise voltages seems to indicate that a field resolution of 22 μT over a 5 MHz bandwidth is possible, with an MT of a mere 6 %/T sensitivity operating in the differential mode and with less than 1 mA of total current. These low noise features together with their high resolution, low power requirements, and ease of fabrication using standard IC technology, makes the magnetotransistor attractive for practical sensing applications.

Having gained adequate knowledge of the MT's operating principles as well as its unique noise properties, one can now proceed to optimise the signal-to-noise ratio of the MT

with respect to its structure and geometry for given fabrication and bias conditions. The optimisation of the device sensitivity can be performed using either numerical or experimental techniques. Numerical modeling is desirable since it reduces by a considerable margin the manpower costs that are involved in the trial and error steps of experimental device development. Furthermore, the costs of computational hardware are steadily declining.

Systems on silicon is the current trend in the demands imposed by the market. The applications communities have keen interests on low cost, high performance and highly reliable integrated system which also features sensing, signal processing, and transmission capabilities on the same chip. With the fast emerging ASIC (Application Specific Integrated Circuit) technology, and in particular with bipolar analog ASIC's that is currently in development, the realisation of such an integrated system on silicon seems feasible in the near future. There are however several steps involved and key technological problems that have to be solved.

Standard structures of sensing elements have to be incorporated as an integral part of the master slice gate array or preferably in the standard cell library. For the case of magnetic sensors, this can be achieved without any additional mask charges while other sensors may require additional post processing steps. It is desirable to condition the output signal of the sensor and convert it into a computer compatible form or into any other form depending on the nature of the application environment. Hence, appropriate cells such as analog to digital converters (and vice versa), operational amplifiers, comparators, buffer amplifiers, filters, etc., have to be made available. Analog cells which are performance optimised can be achieved by incorporating additional steps in the fabrication process, although this may result in an increase in manufacturing costs. Finally, an expedient circuit simulator has to be developed that handles the combination of the analog and digital circuits as well as the output response of the sensing element, without an unacceptable loss of accuracy nor demanding a design environment which from the computational perspective, is unacceptably intensive. With respect to the sensing element, its output response can generally be represented in the form of current, voltage, resistance, or capacitance, viz., ΔI, ΔV, ΔR, and ΔC respectively. To name a

few examples, magnetic field sensors typically provide an output signal of the form ΔI or ΔV, pressure sensors yield either ΔR or ΔC, humidity sensors typically provide ΔC, and light sensors provide ΔI or ΔV. The dependence of the various forms of the output on the external signal (such as magnetic field, pressure, etc.,), can be characterised as variable circuit elements of the type: current sources, voltage sources, resistors, or capacitors. Consequently, the sensor can be replaced by an equivalent circuit that contains the variable circuit element and a sensless device configured in a suitable form, thus making it compatible to analog circuit simulators.

REFERENCES

[1] Lj. Ristić, H. P. Baltes, T. Smy, and I. Filanovsky, "Suppressed sidewall injection magnetotransistor with focused emitter injection and carrier double deflection," *IEEE Electron Device Letts.*, vol. EDL-8, pp. 395-397, 1987.

[2] J. I. Goicolea and R. S. Muller, "Highly sensitive silicon carrier-domain magnetometer," *Sensors and Actuators*, vol. 5, pp. 147-167, 1984.

[3] K. Maenaka, H. Fujiwara, T. Ohsakama, M. Ishida, T. Nakamura, A. Yoshida, and Y. Yasuda, "Integrated magnetic vector sensor," *Proc. 5th Sensor Symp.*, S. Kataoka, Ed., IEE Japan, pp. 179-183, 1985.

[4] S. Kordić, "Integrated 3-d magnetic sensor based on an n-p-n transistor," *IEEE Electron Device Letts.*, vol. EDL-7, pp. 196-198, 1986.

[5] H. P. Baltes and R. S. Popović, "Integrated semiconductor magnetic field sensors," *Proc. IEEE*, vol. 74, No. 8, pp. 1107-1132, 1986.

[6] A. Nathan, H. P. Baltes, D. R. Briglio, and M. Doan, "Noise correlation in dual-collector magnetotransistors," *IEEE Trans. Electron Devices*, submitted.

[7] K. Maenaka, T. Ohgusu, M. Ishida, and T. Nakamura, "Integrated magnetic sensors detecting x, y, and z components of the magnetic field," *Technical Digest, Transducers '87*, Tokyo, Japan, June 2-5, pp. 523-526, 1987.

[8] K. Maenaka, T. Ohsakama, M. Ishida, and T. Nakamura, "An experimental investigation of the operating principles in vertical magnetotransistors," *Sensors and Actuators*, in press.

[9] A. Nathan, W. Allegretto, and H. P. Baltes, "Galvanomagnetic transport in p-n junctions," *Sensors and Materials*, in press.

[10] V. Zieren, "Integrated silicon multicollector magnetotransistors," Ph.D. dissertation, Delft University of Technology, Delft, The Netherlands, 1983.

[11] A. W. Vinal and N. A. Masnari, "Operating principles of bipolar magnetotransistors," *IEEE Trans. Electron Devices*, vol. ED-31, pp. 1486-1494, 1984.

[12] S. Takamiya and K. Fujikawa, "Differential amplification magnetic sensor," *IEEE Trans. Electron Devices*, vol. ED-19, pp. 1085-1090, 1972.

[13] R. S. Popović and H. P. Baltes, "An investigation of the sensitivity of lateral magnetotransistors," *IEEE Electron Device Letts.*, vol. EDL-4, pp. 51-53, 1983.

[14] R. S. Popović and H. P. Baltes, "Dual-collector magnetotransistor optimised with respect to injection modulation," *Sensors and Actuators*, vol. 4, pp. 155-163, 1983.

[15] C. S. Roumenin and P. T. Kostov, "Optimised emitter-injection modulation magnetotransistor," *Sensors and Actuators*, vol. 6, pp. 19-33, 1984.

[16] C. S. Roumenin and M. M. Atanasov, "Magnetotransistor with emitter-injection modulation," *Comptes rendus de l'Academie bulgare des Sciences*, vol. 39, pp. 45-48, 1986.

[17] I. M. Mitnikova, T. V. Persiyanov, G. I. Rekalova, and G. Shtyubner, "Investigation of the characteristics of silicon lateral magnetotransistors with two measuring collectors," *Sov. Phys.-Semicond.*, vol. 12, pp. 26-28, 1978.

[18] S. Selberherr, *Analysis and Simulation of Semiconductor Devices*, Vienna: Springer-Verlag, 1984.

[19] O. Madelung, *Introduction to Soli[illegible]e Theory*, Berlin: Springer-Verlag, 1978.

[20] H. B. Callen, *Thermodynamics*, 2nd reprint, New York: Wiley, 1961.

[21] A. C. Beer, *Galvanomagnetic Effects in Semiconductors*, New York: Academic Press, 1963.

[22] W. Hänsch and F. [illegible], "On the physical problems in process and device simulation: Possibilities and limitations," in *The Interfaces and Integration of Process Device and Circuit Models -An Introduction*, J. J. H. Miller, Ed., Dublin: Boole Press, 1987.

[23] W. Allegretto, A. Nathan, and H. P. Baltes, "Two-dimensional numerical analysis of silicon bipolar magnetotransistors," *Proc. NASECODE V Conference*, June 17-19, J. J. H. Miller, Ed., Dublin: Boole Press, 1987, pp. 87-92.

[24] D. M. Caughey and R. F. Thomas, "Carrier mobilities in silicon empirically related to doping and field," *Proc. IEEE*, vol. 52, pp. 2192-2193, 1967.

[25] G. Baccarani, M. Rudan, R. Guerrieri, and P. Ciampolini, "Physical models for numerical device simulation," in *Process and Device Modeling*, W. L. Engl, Ed., Amsterdam: North Holland, pp. 107-158, 1986.

[26] W. L. Engl, H. K. Dirks, and B. Meinerzhagen, "Device modeling," *Proc. IEEE*, vol. 71, pp. 10-33, 1983.

[27] B. Delauney, "Sur la sphère vide," *Bull. Acad. Science USSR (VII), Classe Sci., Mat. Nat.*, 1934, pp. 793-800.

[28] I. Babuska and A. K. Aziz, "On the angle condition in the finite element method," *SIAM Journal of Numerical Analysis*, vol. 13, 1976, pp. 214-216.

[29] B. J. McCartin, "Discretisation of the semiconductor device equations," in *New Problems and New Solutions for Device and Process Modeling*, J. J. H. Miller, Ed., Dublin: Boole Press, 1985.

[30] M. Rudan, R. Guerrieri, P. Ciampolini, and G. Baccarani, "Discretisation strategies and software implementation for a general-purpose 2D-device simulator," in *New Problems and New Solutions for Device and Process Modeling*, J. J. H. Miller, Ed., Dublin: Boole Press, 1985.

[31] O. C. Zienkiewicz, *The Finite Element Method*, 3rd ed., McGraw-Hill, New York, 1977.

[32] G. Strang and G. F. Fix, *An Analysis of the Finite Element Method*, Prentice-Hall, Englewood Cliffs, New Jersey, 1973.

[33] P. E. Cottrell and E. M. Buturla, "Two-dimensional static and transient simulation of mobile carrier transport in a semiconductor," *Proc. NASECODE I Conf.*, B. T. Browne and J. J. H. Miller, Eds., Dublin: Boole Press, 1979, pp. 31-64.

[34] D. L. Scharfetter and H. K. Gummel, "Large-signal analysis of a silicon read diode oscillator," *IEEE Trans. Electron Devices*, vol. ED-16, pp. 64-77, 1969.

[35] H. K. Gummel, "A self consistent iterative scheme for one-dimensional steady state transistor calculations," *IEEE Trans. Electron Devices*, vol. ED-11, 1964, pp. 455-465.

[36] R. E. Bank and D. J. Rose, "Parameter selection for Newton-like methods applicable to nonlinear partial differential equations," *SIAM Journal of Numerical Analysis*, vol. 17, pp. 806-822, 1980.

[37] T. I. Seidman and S. C. Choo, "Iterative scheme for computer simulation of semiconductor devices," *Solid-State Electronics*, vol. 15, 1972, pp. 1229-1235.

[38] A. George and J. W. H. Liu, "The design of a user interface for a sparse matrix package," *ACM Trans. on Math Software*, vol. 5, pp. 139-162, 1979.

[39] A. Nathan, K. Maenaka, W. Allegretto, H. P. Baltes, and T. Nakamura, "The Hall effect in magnetotransistors," *IEEE Trans. Electron Devices*, submitted.

[40] A. Nathan, W. Allegretto, W. B. Joerg, and H. P. Baltes, "Numerical modeling of bipolar magnetotransistors," *Technical Digest, Transducer's 87*, Tokyo, June 2-5, 1987, pp. 519-522.

[41] D. R. Briglio, *Characterisation of CMOS Magnetic Field Sensors*, M.Sc. Thesis, University of Alberta, Edmonton, Canada, 1988.

[42] C. S. Roumenin, "Hall effect in diode structures," *Comptes rendus de l'Academie bulgare des Sciences*, vol. 38, 1501-1504, 1985.

[43] T. G. M. Kleinpenning, "Design of an a.c. micro-Gauss sensor," *Sensors and Actuators*, vol. 4, pp. 3-9, 1983.

[44] M. Tacano, Y. Sugiyama, and T. Taguchi, "1/f noise in (AlGa)As/GaAs heterostructure Van der Pauw element," *IEEE Electron Device Letts.*, vol. EDL-8, pp. 22-23, 1987.

[45] A. Chovet, S. Christoloveanu, A. Mogaghegh, and A. Dandache, "Noise limitations of magnetodiodes," *Sensors and Actuators*, vol. 4, pp. 147-153, 1983.

[46] A. W. Vinal, "A magnetic sensor utilising an avalanching semiconductor device," *IBM Jour. Res. and Dev.*, vol. 25, pp. 196-201, 1981.

[47] R. S. Popović and R. Widmer, "Sensitivity and noise of a lateral bipolar magnetotransistor in CMOS technology," IEDM 1984, *Technical Digest*, IEEE, pp. 568-571, 1984.

[48] Y. Netzer, "The design of low-noise amplifiers," *Proc. IEEE*, vol. 69, No. 6, pp. 728-741, 1981.

[49] A. Gnudi, P. Ciampolini, R. Guerrieri, M. Rudan, and G. Baccarani, "Sensitivity analysis for device design," *IEEE Trans. Computer-Aided Design*, vol. CAD-6, pp. 879-885, 1987.

APPENDIX 1. PARTIAL LINEARISATION OF CONTINUITY EQUATIONS

In the presence of heavy recombination, the solutions to the continuity equations using the decoupled scheme may yield nonphysical values of the carrier concentrations. It has been shown in [37] that a partial linearisation of the recombination term yields successful solutions to the continuity equations, even under high injection conditions using the decoupled scheme. Furthermore, the increase in computational effort from that required by the usual decoupled approach is only marginal. In the following section, an outline of the procedure applied to the magnetic field dependent transport equations is presented.

For convenience, the electron and hole continuity equations can be expressed in terms of the variables $u = n \exp(-\psi/V_t)$ and $v = p \exp(\psi/V_t)$:

$$\text{div}\, J_{nB} = \text{div}\,[qD_n \beta_n^{-1} \exp(\psi/V_t)\, \text{grad}\, u] = q(uv - n_i^2)/D \qquad \text{(A1.1)}$$

$$\text{div}\, J_{pB} = \text{div}\,[-qD_p \beta_p^{-1} \exp(-\psi/V_t)\, \text{grad}\, v] = -q(uv - n_i^2)/D \qquad \text{(A1.2)}$$

where $D = [\tau_n(p + p_o) + \tau_p(n + n_o)]$ and the rest of the notation as in Section 4.1. Linearising eqns. (A1.1) and (A1.2) around u^o and v^o respectively, results in

$$\text{div}\,[qD_n \beta_n^{-1} \exp(\psi^o/V_t)\, \text{grad}\, u] - u\,(qv^o/D^o) = -qn_i^2/D^o \qquad \text{(A1.3)}$$

$$\text{div}\,[-qD_p \beta_p^{-1} \exp(-\psi^o/V_t)\, \text{grad}\, v] + v\,(qu^o/D^o) = qn_i^2/D^o \qquad \text{(A1.4)}$$

where ψ^o and D^o carry the most recent updates. The box scheme is applied to eqns. (A1.3) and (A1.4), and for node i the respective electron and hole continuity equations in terms of n and p read

$$F_n^T [U^{-1}]^T [\beta_n^{-1}]^T U^T D - \int_A n\,(qp^o/D^o)\, dA = \int_A -qn_{ii}^2/D^o\, dA \qquad \text{(A1.5)}$$

$$F_p^T [U^{-1}]^T [\beta_p^{-1}]^T U^T D + \int_A p\,(qn^o/D^o)\, dA = \int_A qn_{ii}^2/D^o\, dA \qquad \text{(A1.6)}$$

where the various symbols carry the same meaning as in Section 4.1.

APPENDIX 2. PROCEDURE FOR PREDICTING TRIAL VALUES OF POTENTIALS

As discussed in Section 4.2, the solutions to the variables for a desired operating point is obtained by incrementing the applied voltage in steps using knowledge of previous solutions to develop trial values for the subsequent bias point. At medium to high injection levels however, due to the increased coupling of the variables, the procedures presently used seem to genetrate unsatisfactory trial values, unless the step size employed is very small. Small step sizes lead to increased computational demands.

An alternate procedure which could possibly yield more accurate trial values (for larger bias increments) is outlined below. The procedure is somewhat similar to the technique used in [49] to evaluate the sensitivity of the device's output characteristics to variations in the device's physical or geometrical parameters.

Poisson's equation and the carrier continuity equations can be conveniently written in the form;

$$\mathrm{div}\,(\varepsilon\,\mathrm{grad}\,\psi) - qu\exp(\psi/V_t) + qv\exp(-\psi/V_t) + qN = 0 \qquad \text{(A2.1)}$$

$$\mathrm{div}\,[qD_n\beta_n^{-1}\exp(\psi/V_t)\,\mathrm{grad}\,u] - q(uv - n_i^2)/D = 0 \qquad \text{(A2.2)}$$

$$\mathrm{div}\,[-qD_p\beta_p^{-1}\exp(-\psi/V_t)\,\mathrm{grad}\,v] + q(uv - n_i^2)/D = 0 \qquad \text{(A2.3)}$$

where $u = n\exp(-\psi/V_t) = n_i\exp(-\varphi_n/V_t)$ and $v = p\exp(\psi/V_t) = n_i\exp(\varphi_p/V_t)$. The rest of the symbols in usual notation (see Section 4.1 and Appendix 1). On incrementing the bias voltage, the new values of ψ, u and v at the contact become

$$\bar{\psi} = \bar{\psi}^o + \delta\psi, \qquad \bar{u} = \bar{u}^o + \delta u, \qquad \bar{v} = \bar{v}^o + \delta v, \qquad \text{(A2.4)}$$

where $\bar{\psi}^o$, $\bar{u}^o$, and $\bar{v}^o$ denote the boundary values corresponding to the previous bias point and $\delta\psi$, δu, and δv carry the increment in applied voltage at the contact. The terms δu and δv turn out to be zero since n and p at the contact are independent of the applied voltage ($\delta n = \delta p = 0$). Linearising Poisson's equation (A2.1) around ψ^o and the continuity equations (A2.2), (A2.3)

around u^o and v^o respectively (using the procedure shown in Appendix 1), leads to the following system

$$\text{div}\,(\varepsilon\,\text{grad}\,\psi) = qu^o\,[\delta\psi\,V_t + 1]\,\exp(\psi^o/V_t) + qv^o\,[\delta\psi\,V_t - 1]\,\exp(-\psi^o/V_t) - qN$$

$$\text{div}\,[qD_n\,\beta_n^{-1}\,\exp(\psi^o/V_t)\,\text{grad}\,u] = q(u^o v^o - n_i^2)/D^o$$

$$\text{div}\,[-\,qD_p\,\beta_p^{-1}\,\exp(-\psi^o/V_t)\,\text{grad}\,v] = -\,q(u^o v^o - n_i^2)/D^o \qquad \text{(A2.5)}$$

where ψ^o, u^o, and v^o are solutions obtained previously under boundary conditions $\bar{\psi}^o$, $\bar{u}^o$, and $\bar{v}^o$. System (A2.5) is comprised of three linear equations and are to be solved successively under boundary conditions $\bar{\psi}$, $\bar{u}$, and $\bar{v}$. The resulting solutions serve as trial values for the solution of the subsequent bias point. Since the numerical values of most coefficients in system (A2.5) are known *apriori*, the overall computational requirements with this approach are expected to be less than that of the guessing procedure that is currently employed.